

Conservation of radial actions in time-dependent spherical potentials

Jan D. Burger^{1*}, Jorge Peñarrubia² and Jesús Zavala¹

¹*Centre for Astrophysics and Cosmology, Science Institute, University of Iceland, Dunhagi 5, 107 Reykjavík, Iceland*

²*Institute for Astronomy, University of Edinburgh, Royal Observatory, Blackford Hill, Edinburgh EH9 3HJ, UK*

Accepted XXX. Received YYY; in original form ZZZ

ABSTRACT

In slowly evolving spherical potentials, $\Phi(r, t)$, radial actions are typically assumed to remain constant. Here, we construct dynamical invariants that allow us to derive the generic evolution of radial actions in spherical central potentials with an arbitrary time dependence. We show that the radial actions oscillate around a constant value with an amplitude $\Delta J_r \propto \dot{\Phi}/\Phi P(E, L)$, where P is the radial period of an orbit with energy E and angular momentum L . Using this result, we develop a diffusion theory that describes the evolution of the radial action distribution of ensembles of tracer particles orbiting in time-dependent spherical potentials. Tests against restricted N -body simulations in a varying Keplerian potential indicate that our linear theory is accurate in regions of phase-space in which the diffusion coefficient $\tilde{D}(J_r) < 0.01 J_r^2$. For illustration, we show that i) in Milky Way (MW) dark matter haloes with a median mass accretion history only ~ 40 per cent of halo particles evolve within the linear regime since the redshift of maximum accretion, which calls against using radial actions as ‘adiabatic invariants’ when attempting to theoretically predict the density profiles of DM haloes, or construct models for tidal streams in action-angle space. ii) In contrast, the cusp-core transformation of dwarf haloes in self-interacting dark matter (SIDM) models (with $\sigma/m_\chi = 1 \text{ cm}^2 \text{ g}^{-1}$) leads to haloes in which more than ~ 97 per cent of DM particles exhibit a linear behaviour of radial actions. We conclude that the radial action distribution of stellar tracers in SIDM haloes is hardly affected by self-collisions in the dark sector.

Key words: dark matter – stars: kinematics and dynamics

1 INTRODUCTION

The development of a theoretical framework to describe the average dynamics of a large number of particles in the presence of long range forces remains a challenge to this day. Any attempt to model a system of self-gravitating particles using statistical mechanics is met with a number of difficulties. For one, particles interacting with each other gravitationally have negative specific heat (Antonov 1961, Lynden-Bell & Lynden-Bell 1977, Padmanabhan 1989; for a review see Lynden-Bell 1999). Because of this, two gravitationally interacting systems of different initial temperatures will increase their temperature difference throughout the interaction instead of decreasing it. As a consequence, the evolution of systems of particles which are subject to long range forces cannot be described using canonical or grand canonical ensembles. Another property which is specific to large systems of particles which interact via the gravitational force and are not in dynamical equilibrium is non-ergodicity (Lynden-Bell 1999), which implies that the time-average and the ensemble average of dynamical quantities are not equivalent. A further problem was highlighted by Padmanabhan (1990) who argued that the long range nature of the gravitational force forbids the division of the system into non-interacting macrocells, since the en-

ergy of the system is now non-extensive. As a result of this, gravitating systems cannot be described by standard thermodynamics, a conclusion which has been supported by Levin et al. (2008) and Levin et al. (2014).

Despite these challenges, several attempts have been made to derive a valid statistical description of collision-less systems under gravity. Lynden-Bell (1967) sought to construct the equilibrium distribution function of a particle ensemble subject to a strongly time-dependent gravitational force of a newly formed galaxy. The author finds that in general, the most probable coarse-grained distribution function of said particle ensemble is that of a Fermi-Dirac gas, save a normalization factor. In the non-degenerate limit, which is applicable for galaxies, this distribution function can be approximated as a Maxwell-Boltzmann distribution, i.e. the distribution function of an isothermal sphere. The Maxwell-Boltzmann distribution is also obtained by Nakamura (2000) in a different approach using Jaynes (1957) information theory. This result is problematic for two reasons. Not only does it fail to reproduce numerical experiments of violent relaxation (Arad & Johansson 2005), it also implies that the system of particles has an infinite total mass.

While a successful statistical description of violent relaxation of collision-less systems subject to gravitational forces has largely remained elusive, N -body simulations of the evolution of a Universe where most of the matter is made of

* E-mail: jdb5@hi.is (JB)

collision-less cold dark matter (CDM), have been very successful in predicting the large scale structure of the Universe (e.g. [Springel et al. 2005](#)) Another prediction obtained from N -body simulations is the internal spatial structure (commonly represented by a spherically averaged radial density profile) of the gravitationally self-bound virialized objects called haloes, which are the end result of the cosmological process of gravitational accretion and collapse. [Navarro et al. \(1996b\)](#) and [Navarro et al. \(1997\)](#) found that the inner structure of the density profile of these haloes can be described using a single functional form for all resolved halo masses. This so-called Navarro-Frenk-White (NFW) profile is characterized by a central density cusp with a logarithmic slope of -1 . This slope then slowly changes to a value of -3 in the outer regions of the halo. [Navarro et al. \(2010\)](#) showed that the match to the data obtained from N -body simulations can be improved using an Einasto profile instead of an NFW profile (see [Zavala & Frenk \(2019\)](#) for a recent review on DM haloes). Recently, [Wang et al. \(2020\)](#) have shown that N -body simulations lead to universal density profiles over 20 orders of magnitude in halo mass.

In an attempt to derive this universal halo density profile theoretically, [Pontzen & Governato \(2013\)](#) constructed an equilibrium distribution function of particles in DM haloes, using a maximum entropy approach while imposing the additional constraint that radial actions must be conserved. Following arguments by [Jaynes \(1957\)](#), the authors state that statistical mechanics can still be applied to gravitating systems, provided that additional physical constraints other than just the conservation of energy are taken into account. While their approach does work reasonably well over several orders of magnitude, they find that they need to include a second population of particles in order to accurately predict the abundance of particles with very low angular momentum in DM haloes. For instance, their Fig. 7 shows that the inner cusp of DM haloes cannot be explained if this second population of particles with low angular momenta is not added to the first one. In other words, they find that a maximum entropy approach for a single particle population with the additional constraint of conserved radial actions predicts an inner slope of CDM haloes which is not in agreement with N -body simulations.

While the density profiles of haloes predicted by N -body simulations within the CDM model are consistent with observations on most scales, potential challenges to CDM arise on the scale of dwarf galaxies (see [Bullock & Boylan-Kolchin 2017](#) for a recent review). Proposed solutions to these challenges either rely on baryonic physics or alternative DM physics. One particular problem is the so-called cusp-core problem, i.e., the observation that for some dwarf galaxies, cored inner density profiles seemingly provide better agreement with observations than the cuspy NFW-like profile predicted by CDM ([Moore 1994](#), [de Blok et al. 2008](#), [Kuzio de Naray et al. 2008](#), [Walker & Peñarrubia 2011](#)). Supernova-driven gas blowouts can potentially be efficient enough to cause a substantial redistribution of dark matter from the halo centre outward, creating a dark matter core (e.g. [Navarro et al. 1996a](#); [Pontzen & Governato 2012](#)). A possible alternative to the CDM model which can solve the cusp-core problem is self-interacting DM (SIDM, [Spergel & Steinhardt 2000](#), [Yoshida et al. 2000](#), [Davé et al. 2001](#), [Colín et al. 2002](#), [Vogelsberger et al. 2012](#), [Rocha et al. 2013](#)), provided the

SIDM transfer cross section per unit mass σ/m is of the right magnitude $\sim 1\text{cm}^2\text{g}^{-1}$ ([Zavala et al. 2013](#), [Kaplinghat et al. 2016](#)). Currently, both supernova feedback and SIDM are viable mechanisms to create dark matter cores, and thus, it is increasingly relevant to find observables that can distinguish these scenarios. [Burger & Zavala \(2019\)](#) demonstrates that while there are adiabatic and impulsive ways of transforming a CDM cusp into a core, the underlying physical processes imprint distinct signatures into the orbits of kinematic tracers, which might make it possible to distinguish different core formation scenarios. In particular, [Burger & Zavala \(2019\)](#) chose SIDM as an example of an adiabatic scenario of cusp-core transformation. The authors showed that the radial action distribution of stars orbiting in a dwarf-size SIDM halo is approximately conserved, in stark contrast to the substantial evolution observed in the impulsive core formation driven by supernova-feedback.

It is in this context that we investigate in detail under which conditions radial actions can be considered to be truly conserved quantities in time-dependent potentials of astronomical interest. In this article, we closely follow the work presented in [Peñarrubia \(2013\)](#) and [Peñarrubia \(2015\)](#). [Peñarrubia \(2013\)](#) generalized an argument of [Lynden-Bell \(1982\)](#), who found a coordinate transformation relating the equations of motion in Dirac's cosmology with a time-dependent gravitational constant G to the standard equations of motion in a frame in which G is constant. [Peñarrubia \(2013\)](#) showed that using a similar coordinate transformation, the equations of motion of particles orbiting in any time-dependent central potential can be solved in a frame in which the potential is static, provided that one is able to solve an auxiliary differential equation for a scale-factor R . This scale-factor relates the radius r in the frame in which the potential evolves with time to the radius r' in the frame in which the potential is static via $r = Rr'$. If the scale-factor R is known, it is possible to define dynamical invariants, which are the integrals of motion in the frame in which the potential is static. In a subsequent paper, [Peñarrubia \(2015\)](#) showed that if the evolution of the potential is slow enough, it is possible to predict the evolution of the energy distribution of particles orbiting in a time-dependent potential. This is done by deriving a diffusion formalism which relates the energy distribution to the distribution of invariant energies in the static frame. The task of obtaining the energy distribution at a given time t is then reduced to the calculation of drift and diffusion coefficients $\tilde{C}(E, t)$ and $\tilde{D}(E, t)$. This approach to statistical mechanics allows for a definition of micro-canonical particle ensembles using dynamical invariants and does not rely on the assumption of ergodicity. In this article we extend this formalism to the radial action space.

Our paper is structured as follows: In Section 2, we derive the first order Taylor expansion of the time-dependent radial action J_r in the parameter \dot{R}/R . We thus provide a general expression for the linear oscillation amplitude ΔJ_r , which equals the difference between J_r and the invariant action J'_r , as long as the potential evolves slowly enough for the first order Taylor expansion to be valid. We then follow the orbits of three different tracer particles in a time-dependent Keplerian potential to show that the first-order Taylor expansion provides a good description of the evolution of J_r provided ΔJ_r is small. In Section 3, we derive the diffusion equation in radial action space and define drift and diffusion coefficients $\tilde{C}(J_r, t)$

and $\tilde{D}(J_r, t)$. Furthermore, we show that we can classify the evolution of radial action distributions as linear or non-linear, depending on whether $\sqrt{\tilde{D}} \ll J_r$ or $\sqrt{\tilde{D}} \geq J_r$. In Section 4, we perform restricted N -body simulations of five different tracer particle ensembles in a time-dependent Keplerian potential. All of the tracer ensembles initially follow a Gaussian distribution in radial action. We then use the diffusion formalism to predict the time-evolution of each of the radial actions distributions and test whether the diffusion formalism yields accurate results, both in cases where $\sqrt{\tilde{D}} \ll J_r$ (linear) and in cases where $\sqrt{\tilde{D}} \sim J_r$ (non-linear) on average. Based on the results obtained in Section 4, in Section 5 we discuss whether or not radial actions can be considered conserved quantities in Milky-Way (MW) size CDM haloes. To this end, we apply our formalism using the median mass accretion history of MW size haloes reported in [Boylan-Kolchin et al. \(2010\)](#) to estimate the fraction of DM particles within the MW halo whose radial actions are expected to show a linear rather than a non-linear evolution. Furthermore, we also perform an N -body simulation of a dwarf-size halo which is forming a core due to self-scattering between its DM particles. For a dwarf-size halo with $\sigma/m_\chi = 1 \text{ cm}^2 \text{ g}^{-1}$, we quantify how adiabatic core formation proceeds by calculating the fraction of particles within the virial radius of the halo whose radial actions evolve in the linear regime. In addition, we apply the diffusion formalism developed in Section 3 to predict the evolution of an initially Gaussian radial action distribution of tracer particles. We draw our conclusions in Section 6. Appendix A outlines how the scale factor is calculated numerically, Appendix B discusses a modification to the diffusion formalism developed in Sections 2 and 3, and in Appendix C we discuss an approximation to the scale factor in potentials that are not scale-free.

2 RADIAL ACTIONS IN A TIME-DEPENDENT POTENTIAL

2.1 Time-dependent radial action distributions

The radial action is an integrals of motion in spherical static potentials ([Binney & Tremaine 1987](#)). It is defined as

$$J_r = \frac{1}{\pi} \int_{r_{\text{peri}}}^{r_{\text{apo}}} dr \sqrt{2[E - \Phi(r)] - \frac{L^2}{r^2}}, \quad (1)$$

where E denotes the particle's energy, L its angular momentum and $r_{\text{peri,apo}}$ the peri- and apocentre of the particle's orbit. In a spherically symmetric potential, the peri- and apocentre radii are functions of energy and angular momentum only. If the potential is static, both energy and angular momentum are integrals of motion and thus the radial action itself is an integral of motion as well.

If the potential varies with time while retaining its spherical symmetry, [Binney & Tremaine \(1987\)](#) argue that radial actions remain approximately constant insofar as the change is 'slow'. For this reason, radial actions are often called adiabatic invariants. The question of exactly how slow the change in potential has to be for this to hold true is, however, non-trivial. In this paper, we aim to answer this question by developing a diffusion formalism that describes the evolution of radial action distributions of particle ensembles orbiting

in a time-dependent potential. The computation of radial actions typically requires orbital integration using numerical tools. Keplerian potentials are an exception to this rule, in the sense that they allow an analytical derivation of radial actions. Because of this, and in order to gain physical insight into this problem, we focus primarily on the case of particles moving in a Keplerian potential that varies with time,

$$\Phi(r, t) = -\frac{GM(t)}{r}, \quad (2)$$

In this case, the integral in Eq. (1) is analytic and we can write the radial action as (e.g. [Goodman & Binney 1984](#))

$$J_r = \frac{GM}{\sqrt{-2E}} - L \quad (3)$$

Equipped with Eq. (3) as an analytic formula for the radial action, we run a simple test simulation of 10^5 tracer particles orbiting in a time-dependent Keplerian potential with a linear time dependence on the mass

$$\Phi(r, t) = -\frac{GM_0(1 + \epsilon t)}{r} \quad (4)$$

and with initial phase space coordinates chosen at random. For computational efficiency, we demand the initial orbital radius to be smaller than $300h^{-1} \text{ kpc}$ and that the angular momentum of each particle is smaller than $150h^{-1} \text{ kpc km s}^{-1}$. This is done in order to avoid very extended and energetic orbits. For definiteness, we choose $M_0 = 10^8 h^{-1} M_\odot$ and $\epsilon = 1/30 h \text{ Gyr}^{-1}$ in Eq. (4). All of the results presented in this paper are derived using these values for the two model parameters.

We then treat Eq. 4 as an external potential that varies slowly. In particular, the Keplerian mass in our models grows by 10 per cent over $3h^{-1} \text{ Gyr}$. Next, we solve the equations of motion of tracer particles in the time-dependent potential using the N -body part of AREPO ([Springel 2010](#)), and compute their radial actions from their phase space coordinates following Eq. (3). Radial action distributions are measured at different times, which provides a qualitative description of the conservation of radial actions in different regions of the orbital distribution allowing us to test the expectation that radial actions are indeed adiabatic invariants.

In Fig. 1, we show the evolved radial action distribution at two different times: $t = 300h^{-1} \text{ Myr}$ (left panel), and $t = 3h^{-1} \text{ Gyr}$ (right panel). In the upper part of each panel, we show the current distribution $N(J_r, t)$ as a red solid line and the distribution at $t = 0$ as a black dotted line. We also show the radial action distribution in a frame where the host potential is kept constant as a green dashed line. In the bottom part of each panel, we present the fractional change in the distribution $\delta N(J_r, t)$, defined as

$$\delta N(J_r, t) = \frac{N(J_r, t) - N(J_r, 0)}{N(J_r, 0)}. \quad (5)$$

We find almost no evolution when using a static Keplerian potential, as should be the case, since actions are integrals of motion. In the simulation with a time-dependent host potential, however, we see a striking evolution of the radial action distribution. As time goes by, we observe a progressive flattening of the distribution's tail at $J_r > 100h^{-1} \text{ kpc km s}^{-1}$. At larger values, we find that $\delta N(J_r, t)$ slowly tends towards the limiting value of -1 at $J_r = 300h^{-1} \text{ kpc km s}^{-1}$, indicating that there are almost no particles left with radial actions

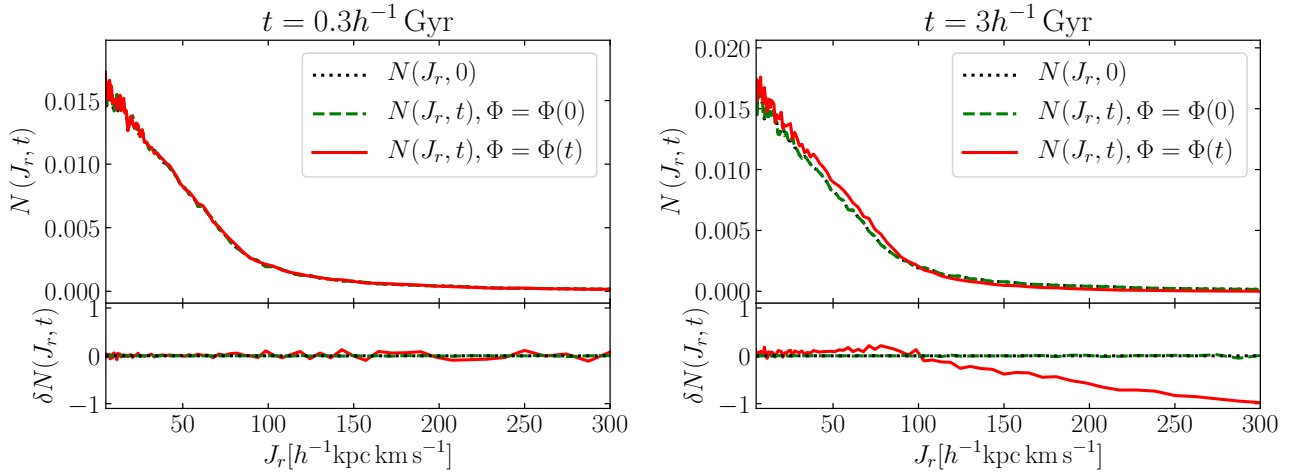


Figure 1. Evolution of the radial action distribution calculated from the orbits of 10^5 tracer particles in a time-dependent Keplerian potential (see Eq. 4). The black dotted lines show the initial distribution, the dashed green lines show the distribution evolved in a frame with a static potential, and the solid red lines show the distribution in the time-dependent frame. The simulation times at which the distributions are measured are indicated in the title of each panel. The top of either panel shows the distribution, whereas the bottom shows the fractional change in the distribution with respect to the initial distribution. When evolving the distribution from 0.3 to 3 h^{-1} Gyr, we find that the lower end of the distribution increases in the simulation with a time-dependent potential, while we witness an opposite trend at larger action values, indicating a net drift of radial actions from larger to smaller values.

larger than that. As a result of this, we find that $\delta N(J_r, t)$ is continuously larger than 0 at radial actions smaller than $100 h^{-1} \text{ kpc km s}^{-1}$. Overall, this indicates a significant net drift of the initial distribution towards smaller radial actions.

2.2 First-order expansion of time-dependent radial actions

To describe the evolution of the radial action distribution seen above, we turn to the formalism of dynamical invariants developed in Peñarrubia (2013), which is based on a coordinate transformation found by Lynden-Bell (1982). In a time-dependent potential, particles are subject to a time-dependent force

$$\ddot{\mathbf{r}} = \mathbf{F}(\mathbf{r}, t). \quad (6)$$

If the force is conservative, Peñarrubia (2013) and Lynden-Bell (1982) show that for each phase space trajectory there exists a canonical transformation $\mathbf{r} \rightarrow R(t)\mathbf{r}'$ and a complementary transformation of the time coordinate $dt \rightarrow d\tau R^2(t)$ such that the time-dependence vanishes from the equation of motion, which can then be written as

$$\frac{d^2 \mathbf{r}'}{d\tau^2} = \mathbf{F}'(\mathbf{r}') \quad (7)$$

The scale-factor $R(t)$ is then a solution to the differential equation

$$\ddot{R}R^3 \mathbf{r}' - R^3 \mathbf{F}(R\mathbf{r}', t) = -\mathbf{F}'(\mathbf{r}'). \quad (8)$$

Notice that here, the time-evolution of the scale factor is in general coupled to the phase space trajectory. Peñarrubia (2013) shows that in the case of a slowly changing potential, an approximate first-order solution to Eq. (8) exists for scale-free potentials. In general, however, Eq. (8) is coupled with the equations of motion (6) and cannot be solved analytically.

Up to first order in \dot{R}/R , the energy of a particle which is subject to the force in Eq. (6) is

$$E \approx \frac{I}{R^2} + \frac{\dot{R}}{R} (\mathbf{r} \cdot \mathbf{v}), \quad (9)$$

where I is a dynamical invariant equal to the energy in the frame in which Eq. (7) is the equation of motion, i.e., the “time-independent”, or static, frame.

Eq. (9) expresses the energy in the time-dependent frame as a function of the invariant energy and a first order correction that depends on the orbit of each particle. In the following, we aim to derive a similar expression for the radial action. A possible way to do so, presented in Peñarrubia (2013), is to simply insert Eq. (9) into Eq. (3) and identify the first order correction from there. However, since the radial action is not usually analytic in generic spherically symmetric potentials, it is desirable to derive an expression for the first order correction that does not depend on the particle trajectory.

To accomplish this, we start by integrating Eq. (8) on both sides to define

$$\tilde{\Phi}(\mathbf{r}') = - \int d\mathbf{r}' \cdot \mathbf{F}'(\mathbf{r}') = \frac{1}{2} \dot{R} R^3 r'^2 + R^2 \Phi(R\mathbf{r}', t). \quad (10)$$

The radial action in the time-independent frame is

$$J_{r'} = \frac{1}{\pi} \int_{r'_{\text{peri}}}^{r'_{\text{apo}}} dr' \sqrt{2I - 2\tilde{\Phi}(\mathbf{r}') - \frac{L^2}{r'^2}}, \quad (11)$$

where $J_{r'}$ is a dynamical invariant akin to I . We now would like to relate Eq. (11) to the radial action that one would de-facto measure in a time-dependent potential. To measure J_r in a time-dependent frame, one usually fixes the gravitational potential at the time one measures J_r . For this reason, we also call J_r the “instantaneous” action. Fixing Φ at the time we measure J_r , we can define effective apo- and pericentre radii in the time-dependent frame. Formally, this means that we consider quantities in the time-dependent frame at a fixed

time t_1 . At this time, the invariant energy is

$$I = R^2(t_1)E(t_1) - R^2(t_1)\frac{\dot{R}(t_1)}{R(t_1)}(\mathbf{r}(t_1) \cdot \mathbf{v}(t_1)). \quad (12)$$

We then obtain

$$J_{r'} = \frac{1}{\pi} \int_{r'_{\text{peri}}}^{r'_{\text{apo}}} dr' R(t_1) \sqrt{f(\mathbf{r}', t_1)}, \quad (13)$$

where

$$\begin{aligned} f(\mathbf{r}', t_1) = & 2E(t_1) - 2\frac{\dot{R}(t_1)}{R(t_1)}(\mathbf{r}(t_1) \cdot \mathbf{v}(t_1)) \\ & - \ddot{R}(t_1)R(t_1)r'^2 - 2\Phi(R(t_1)\mathbf{r}', t_1) \\ & - \frac{L^2}{R^2(t_1)r'^2}. \end{aligned} \quad (14)$$

Now, we can perform the coordinate transformation $\mathbf{x} = R(t_1)\mathbf{r}'$, which is simply a shift of the radial coordinate. We write the effective apo- and pericentre radii in the time-dependent frame as

$$R(t_1)r'_{\text{apo,peri}} = r_{\text{apo,peri}}(t_1) \quad (15)$$

which is physically exact in the fully adiabatic limit. With these definitions,

$$J_{r'} = \frac{1}{\pi} \int_{r_{\text{peri}}(t_1)}^{r_{\text{apo}}(t_1)} dx \sqrt{f(\mathbf{x}, t_1)} \quad (16)$$

with

$$\begin{aligned} f(\mathbf{x}, t_1) = & 2E(t_1) - 2\frac{\dot{R}(t_1)}{R(t_1)}(\mathbf{r}(t_1) \cdot \mathbf{v}(t_1)) \\ & - \frac{\ddot{R}(t_1)}{R(t_1)}x^2 - 2\Phi(\mathbf{x}, t_1) - \frac{L^2}{x^2}. \end{aligned}$$

In the limit $|\ddot{R}/R| \ll |\dot{R}/R|$ we can perform a Taylor expansion to first order in \dot{R}/R to find

$$\begin{aligned} J_{r'} = & \frac{1}{\pi} \int_{r_{\text{peri}}(t_1)}^{r_{\text{apo}}(t_1)} dx \sqrt{2E(t_1) - 2\Phi(\mathbf{x}, t_1) - \frac{L^2}{x^2}} \\ & - \frac{\dot{R}(t_1)}{R(t_1)}(\mathbf{r}(t_1) \cdot \mathbf{v}(t_1)) \\ & \times \frac{1}{\pi} \int_{r_{\text{peri}}(t_1)}^{r_{\text{apo}}(t_1)} dx \frac{1}{\sqrt{2E(t_1) - 2\Phi(\mathbf{x}, t_1) - \frac{L^2}{x^2}}} \\ & + \mathcal{O}\left(\left[\frac{\dot{R}(t_1)}{R(t_1)}\right]^2, \frac{\ddot{R}(t_1)}{R(t_1)}\right). \end{aligned} \quad (17)$$

Dropping all the higher order terms, this leads to

$$J_{r'} \approx J_{r,t_1} - \frac{\dot{R}(t_1)}{R(t_1)}(\mathbf{r}(t_1) \cdot \mathbf{v}(t_1)) \frac{P(E, L, t_1)}{2\pi} \quad (18)$$

In this equation, both J_{r,t_1} and $P(E, L, t_1)$ refer respectively to instantaneous actions and radial periods measured at the fixed time t_1 . Now, if the system is adiabatic, we can chose t_1 to be any time t and simply write

$$J_r \approx J_{r'} + \frac{\dot{R}}{R}(\mathbf{r} \cdot \mathbf{v}) \frac{P(E, L)}{2\pi} \quad (19)$$

up to linear order in perturbation theory. As long as the change in the potential is slow enough, the quantity $J_{r'}$ in Eq. (19) is a dynamical invariant. In case of a faster change in the potential, higher order terms of the perturbative expansion have to be taken into account until at some point the evolution becomes non-perturbative.

2.3 Individual tracer orbits in a time-dependent Keplerian potential

To begin testing the accuracy and limitations of Eq. (19), we find it useful to follow the orbits of three tracer particles covering a large spectrum of energies, and orbiting in an evolving host potential given by Eq. (4) with $M_0 = 10^8 h^{-1} M_\odot$ and $\epsilon = 1/30 h \text{ Gyr}^{-1}$. The three particles are initially located at $5 h^{-1} \text{ kpc}$ from the host centre, but have different initial energies and angular momenta.

Since negative energies correspond to gravitationally bound particles, let us define $\mathcal{E} = -E$ as our energy variable of reference. In a Keplerian potential, the radial period and the azimuthal period coincide and can, in terms of the energy, be written as

$$P(E, L) \equiv P(\mathcal{E}) = 2\pi \frac{GM}{\sqrt{2\mathcal{E}^3}} \quad (20)$$

Eq. (20) states that in a Keplerian potential, the orbital period is directly determined by the energy of the particle, with more energetic particles having larger periods. Evidently, this implies that in a time-dependent potential, the period is not constant.

Eq. (19) implies that the amplitude with which J_r oscillates around the dynamical invariant $J_{r'}$ is directly related to the orbital period. Moreover, given that the first order correction to $J_{r'}$ has to be small compared to the value of $J_{r'}$ itself for the linear approximation to be valid, we expect that the first order Taylor expansion will become progressively less accurate as $\mathcal{E} \rightarrow 0$. This region is usually known as the ‘‘fringe’’ of a self-gravitating system. As shown below, the evolution of the radial action of particles in the fringe is highly non-perturbative.

We consider three particles with the following energies and angular momenta

$$(\mathcal{E}[\text{km}^2 \text{ s}^{-2}], L[\text{h}^{-1} \text{ kpc km s}^{-1}]) = \{(50, 33), (20, 55), (2, 15)\}. \quad (21)$$

The first two sets are chosen such that the radial actions will be of similar amplitude, allowing us to quantify the impact of the orbital energy on the amplitude of the radial action oscillation and, thus, on the accuracy of Eq. (19). The last set of values leads to a much larger initial radial action and is chosen primarily to illustrate what happens when the linear correction term exceeds the dynamical invariant in magnitude, i.e., when we enter the ‘‘fringe’’ of the potential.

The upper panels of Fig. 2 show the time evolution of the radial actions of the three particles in our experiment. Black lines in each figure denote an exact calculation of the radial action following Eq. (3). Red-dotted and blue-dashed lines both refer to the linear approximation for the radial action given in Eq. (19), using expression (20) to calculate the radial oscillation period. The difference between the latter two cases lies in the way \dot{R}/R is estimated. The scale-factor used to obtain the red line is calculated directly from Eq. (8), using a KDK leapfrog algorithm to solve the differential equation. The scale-factor’s evolution is thus ‘‘coupled’’ to the particle’s phase space trajectory. The dashed blue lines refer to an approximate analytic solution to the scale factor that can be calculated for scale-free potentials, as has been shown in Peñarrubia (2013). In this approximation the equation of motion is ‘‘de-coupled’’ from Eq. (8). A more detailed explanation of the leapfrog solving algorithm, along with a compari-

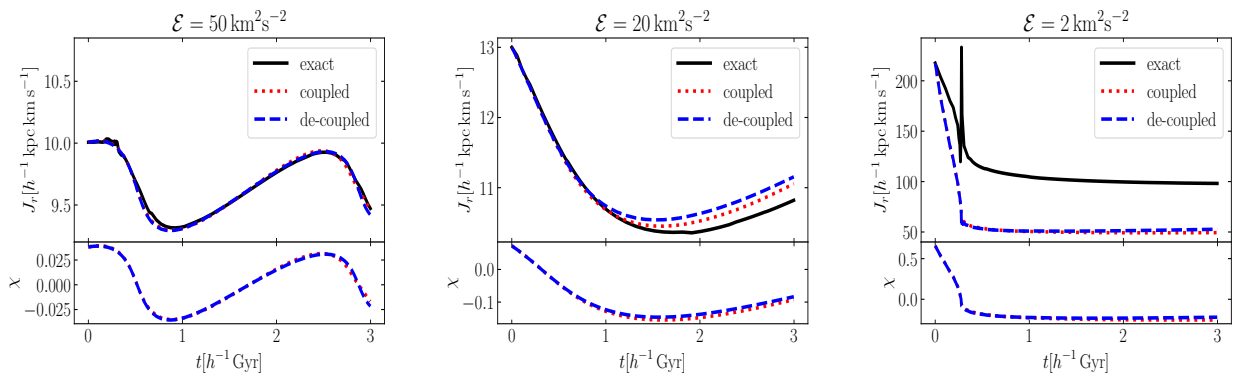


Figure 2. The upper panels show the time evolution of the radial action of three different particles orbiting in a time-dependent Keplerian potential. Initial energies are shown at the top of each plot. Black solid lines denote a direct measurement of the radial action from energies and angular momenta according to Eq. (3). Red dotted lines and blue dashed lines both correspond to the linear approximation given by Eq. (19), using two different estimates for \dot{R}/R . “Coupled” and “de-coupled” refer to an exact (dotted red) or approximate (dashed blue) way of solving Eq. (8). Angular momenta are chosen such that the initial radial actions are around $J_r = 10 h^{-1} \text{ kpc km s}^{-1}$ in the left and middle panel, and around $J_r = 200 h^{-1} \text{ kpc km s}^{-1}$ in the right panel. The lower panels show the ratio χ between the linear approximation and the exact value of the radial action as a function of time.

son between the numerically calculated and the approximate scale-factors can be found in Appendix A.

In the three lower panels of Fig. (2) we show $\chi = \Delta/J_r$, where $\Delta \equiv (\dot{R}/R)(\mathbf{r} \cdot \mathbf{v})P/(2\pi)$. Notice that χ quantifies the fractional size of the first order correction relative to the radial action, and can be positive or negative along the orbital phase.

Comparison of the left and middle panels of Fig. 2 shows that the orbital period is shorter in the left panel, which is in line with our expectation from Eq. (20). Furthermore, the results confirm our expectation that the amplitude of the first order correction increases with the energy at a fixed invariant action. We find that for the most bound particle (left panel), the first order Taylor expansion is an excellent fit to the measured radial action. We furthermore find that there is almost no difference between the red and blue lines, which indicates that the “de-coupled” approximation to the scale-factor provides a good approximation to its true value. The success of the Taylor expansion here is reflected in χ as well, which peaks at ~ 2.5 per cent when the magnitude of the radial velocity is maximal. As the period increases, the agreement between the measured radial action and the prediction from Eq. (19) starts to deteriorate after roughly $1 h^{-1} \text{ Gyr}$ of integration (notice that in the middle panel $|\chi|$ has risen to ~ 10 per cent). Nonetheless, the evolution of the radial action is still captured well by this approximation. We furthermore find that the numerical solution to Eq.(8) now provides a slightly more accurate result than the approximate analytic solution for \dot{R}/R .

The right panel of Fig. 2 shows a particle which is in the “fringe” of the potential, which is evident by χ reaching values as large as 70 per cent. Due to that, we find that the dynamical invariant J_r is not properly defined by the linear approximation. Note that the orbital period of this particle is much longer than the total simulation time, meaning we only resolve a fraction of an orbital revolution. Within this time interval, the radial action undergoes a strongly non-linear fluctuation when the particle passes its orbital pericentre and then quickly settles to a value which is roughly half of its initial value. The linear approximation completely fails to cap-

ture this behaviour. We conclude that the evolution of this particle’s action is both non-adiabatic and non-perturbative.

3 DIFFUSION FORMALISM FOR RADIAL ACTION DISTRIBUTIONS

Based on the first order Taylor expansion for time-dependent radial actions described in the previous section, we now develop a diffusion formalism similar to the one in Peñarrubia (2015) to analytically describe the evolution of radial action distributions. We furthermore aim to differentiate regimes in phase space in which the evolution of radial action distributions is diffusive from regimes in which it is not.

3.1 The diffusion equation for radial action distributions

To derive a diffusion equation for radial actions, we closely follow the formalism presented in Peñarrubia (2015) based on Einstein (1905).

Let us define $\phi(\Delta|J_{r'})d\Delta$ as the conditional probability that a particle with the dynamically invariant action $J_{r'}$ will change its action by an amount Δ in the range $d\Delta$ during the time interval $(t, t + \tau')$; ϕ is normalized such that

$$\int \phi(\Delta|J_{r'})d\Delta = 1. \quad (22)$$

Subsequently, we define $p(J_r, t_0 + \tau'|J_{r'}, t_0)dJ_r$ as the probability that a particle with action $J_{r'}$ at t_0 will have an action in the interval $[J_r, J_r + dJ_r]$ at a later time $t = t_0 + \tau'$. As with the equivalent in energy space presented in Peñarrubia (2015), these two functions obey Einstein’s master equation

$$p(J_r, t_0 + \tau'|J_{r'}, t_0)dJ_r = dJ_r \int p(J_r - \Delta, t_0|J_{r'}, t_0)\phi(\Delta|J_{r'})d\Delta. \quad (23)$$

Now if we are in the adiabatic limit where Eq. (19) applies, or equivalently $\chi = \Delta/J_r \ll 1$, we can expand Eq. (23) in

Δ to find

$$p(J_r, t_0 + \tau' | J_{r'}, t_0) \approx p(J_r, t_0 | J_{r'}, t_0) - \frac{\partial p}{\partial J_r} \Big|_{\Delta=0} \int \phi(\Delta | J_{r'}) \Delta d\Delta + \frac{1}{2} \frac{\partial^2 p}{\partial J_r^2} \Big|_{\Delta=0} \int \phi(\Delta | J_{r'}) \Delta^2 d\Delta. \quad (24)$$

Since we can also expand the lhs of Eq. (24) around $t = t_0$ to first order

$$p(J_r, t_0 + \tau' | J_{r'}, t_0) \approx p(J_r, t_0 | J_{r'}, t_0) + \frac{\partial p}{\partial t} \tau',$$

we then have

$$\frac{\partial p}{\partial t} = C \frac{\partial p}{\partial J_r} \Big|_{\Delta=0} + D \frac{\partial^2 p}{\partial J_r^2} \Big|_{\Delta=0}, \quad (25)$$

where we define the drift coefficient

$$C(J_{r'}, t) = -\frac{1}{\tau'} \int \phi(\Delta | J_{r'}) \Delta d\Delta \quad (26)$$

and the diffusion coefficient

$$D(J_{r'}, t) = \frac{1}{2\tau'} \int \phi(\Delta | J_{r'}) \Delta^2 d\Delta. \quad (27)$$

Analogous to the discussion in Peñarrubia (2015), the initial condition to solve Eq. (25) is $p(J_r, t_0 | J_{r'}, t_0) = \delta(J_r - J_{r'})$ and the general solution to this equation is a Green function

$$p(J_r, t | J_{r'}, t_0) = \frac{1}{\sqrt{4\pi \tilde{D}(J_{r'}, t)}} \times \exp \left\{ -\frac{[J_r - J_{r'} + \tilde{C}(J_{r'}, t)]^2}{4\tilde{D}(J_{r'}, t)} \right\}, \quad (28)$$

the properties of which are discussed in detail in Peñarrubia (2015). In Eq. (28) we have implicitly defined scaled drift and diffusion coefficients $\tilde{C} = C\tau'$, $\tilde{D} = D\tau'$. Note that the fact that \tilde{C} and \tilde{D} are independent of time implies that there is no divergence for short transition times in Eq. (28).

3.2 Drift and diffusion coefficients

Similar to Section 2.3 of Peñarrubia (2015) we now briefly discuss how to calculate the drift and diffusion coefficients defined in Eqs. (26) and (27). To this end, we define a micro-canonical distribution function $w(J_r, E)$ depending on both energy and radial action as

$$w(J_r, E) = \int \delta(J_r - X) \delta(E - H) d^3\mathbf{r} d^3\mathbf{v}, \quad (29)$$

where

$$X = \int_{r_{\text{peri}}}^{r_{\text{apo}}} dr \sqrt{2(E - \Phi(r)) - \frac{L^2}{r^2}}. \quad (30)$$

We then define the drift and diffusion coefficients as micro-canonical averages over the particle distribution as follows

$$\tilde{C}(J_r, E, t) = -\frac{1}{w} \times \int \frac{\dot{R}}{R} (\mathbf{r} \cdot \mathbf{v}) \frac{P(H, X, t)}{2\pi} \delta(J_r - X) \delta(E - H) d^3\mathbf{r} d^3\mathbf{v} \quad (31)$$

$$\tilde{D}(J_r, E, t) = \frac{1}{2w} \times \int \left(\frac{\dot{R}}{R} (\mathbf{r} \cdot \mathbf{v}) \frac{P(H, X, t)}{2\pi} \right)^2 \delta(J_r - X) \delta(E - H) d^3\mathbf{r} d^3\mathbf{v}. \quad (32)$$

Notice that here we have written the period as a function of both the energy and the radial action, which is in general possible as we can express the angular momentum as a function of energy and radial action. In order to calculate a drift and diffusion coefficient that depends only on the radial action, however, we have to integrate over the energies

$$\tilde{C}(J_r, t) = \frac{1}{w(J_r)} \int dE w(J_r, E) \tilde{C}(J_r, E, t) \quad (33)$$

$$\tilde{D}(J_r, t) = \frac{1}{w(J_r)} \int dE w(J_r, E) \tilde{D}(J_r, E, t), \quad (34)$$

where

$$w(J_r) = \int dE w(J_r, E) \quad (35)$$

is the microcanonical distribution function depending only on the radial action. Before integrating out the energy, however, we can use Eqs. (32) and (31) to calculate the area in phase space in which the diffusion approach is applicable. To this end, we use the “de-coupled” analytic expression for the scale-factor. Peñarrubia (2013) shows that in a scale-free potential with a time-dependent force

$$F(r, t) = -\mu(t)r^n, \quad (36)$$

a good analytic approximation to the scale-factor is

$$R(t) \approx \left(\frac{\mu(t)}{\mu(0)} \right)^{-1/(n+3)}. \quad (37)$$

Furthermore, in the case of a Keplerian potential, the period depends only on the energy and it is fixed at a fixed time, thus, we can take it out of the averaging process to obtain:

$$\tilde{C}(J_r, E, t) \approx -\frac{\dot{R}}{R} \frac{P(E)}{2\pi} \langle (\mathbf{r} \cdot \mathbf{v}) \rangle \quad (38)$$

$$\tilde{D}(J_r, E, t) \approx \frac{1}{2} \left(\frac{\dot{R}}{R} \right)^2 \left(\frac{P}{2\pi} \right)^2 \langle (\mathbf{r} \cdot \mathbf{v})^2 \rangle \quad (39)$$

If we now assume that the initial particle distribution is phase-mixed and virialized, we can use the same arguments as in Peñarrubia (2015) and state that to a good approximation $\dot{C} = \partial \tilde{C} / \partial t = 0$, which means that the net drift is zero. Following the Appendix C1 of Peñarrubia (2019), we can write

$$\langle (\mathbf{r} \cdot \mathbf{v})^2 \rangle = \frac{1}{2} \left(2 \frac{GM}{\sqrt{2\mathcal{E}}} J_r - J_r^2 \right) \quad (40)$$

which, making use of Eq. (20), implies that in a Keplerian potential

$$\tilde{D}(J_r, E, t) = \frac{1}{4} \left(\frac{\dot{R}}{R} \right)^2 (GM)^2 \frac{GMJ_r - \sqrt{2\mathcal{E}}J_r^2}{(2\mathcal{E})^{\frac{7}{2}}}. \quad (41)$$

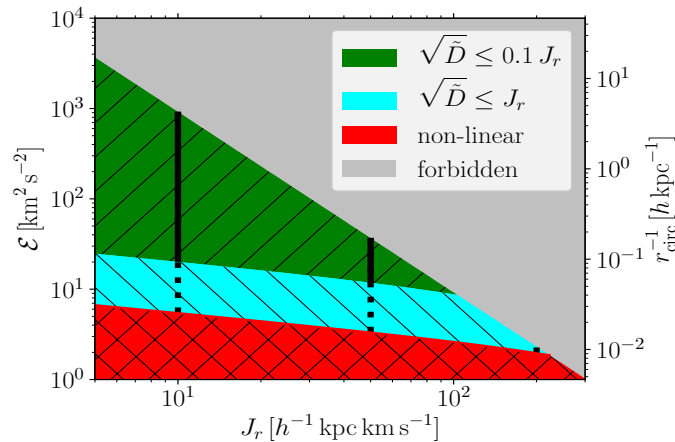


Figure 3. $\mathcal{E} - J_r$ phase space in a time-dependent Keplerian potential. The grey area is not populated, as no particles can exist there according to Eq. (3). The green area denotes the perturbative “linear” regime in which $\sqrt{\tilde{D}} \ll 0.1J_r$. The cyan area denotes a “transition” regime between the “linear” regime and the “fringe”. Here, $0.1 < \sqrt{\tilde{D}}/J_r < 1$. In red, we show the non-linear (“fringe”) part of the phase space. Here, the first order variation can be bigger than the action itself, meaning that the invariant action defined in Eq. (19) is not a dynamical invariant and the diffusion formalism is not applicable. In order to compile this plot, we have used $M_0 = 10^8 h^{-1} M_\odot$, $\epsilon = 1/30 h^{-1} \text{Gyr}$ in Eq. (4), implying $\dot{R}/R = 1/30 h \text{Gyr}^{-1}$ at $t = 0$. On the right y-axis we show the radius of a circular orbit of a particle with energy \mathcal{E} as an indication of the scales involved.

The variance of the probability function (Eq. 28) is $\Delta^2 = 2\tilde{D}$, which means that the diffusion coefficient is closely related to the evolution of the particle distribution. To identify the phase space area in which the diffusion formalism is applicable, we require that $\sqrt{\tilde{D}} \ll J_r$, which implies $\chi \ll 1$. We use Eq. (41) to calculate (theoretical) diffusion coefficients and to define three different areas in the $J_r - \mathcal{E}$ phase space, characterized by $\sqrt{\tilde{D}} < 0.1J_r$, $\sqrt{\tilde{D}} < J_r$ and $\sqrt{\tilde{D}} > J_r$.

Fig. 3 shows a plot of the $\mathcal{E} - J_r$ phase space with the different areas computed from Eqs. (3) and (41) using the same parameters for the time-dependent Keplerian potential as in Section 2.1 at $t = 0$. For reference, we show the radius of a circular orbit with energy \mathcal{E} on the right y-axis.

The grey area is dictated by Eq. (3) and its border corresponds to the line at which $L = 0$. Any allowed orbits are located to the left in one of the coloured areas.

Particles inhabiting the green area have an average diffusion coefficient which is smaller than one per cent of the squared radial action. In this area, the diffusion formalism is applicable.

For particles in the cyan area, the average diffusion coefficient is larger than one per cent of the squared radial action, yet smaller than the squared radial action itself. This represents a “transition” regime between the perturbative regime and the “fringe”.

The red area is the “fringe” of the potential. Here, the evolution of radial actions is highly non-linear and the diffusion formalism is not applicable.

It should be noted that the exact locations of the areas vary with time, as the mass of the Keplerian potential directly im-

pacts all the three boundaries shown in this picture. Furthermore, as not all relevant distributions of tracer particles are phase-mixed and in virial equilibrium, using Eq. (41) along with $\tilde{C} = 0$ is not always a valid approximation. Nonetheless, the areas defined in Fig. 3 give a good indication as to which radial action - energy combinations imply a linear, diffusive evolution and which do not.

We now aim to use the definition of the three phase space areas made in Fig. 3 to investigate whether the flattening of the tail in Fig. 1 is a linear or a non-linear phenomenon. Given that the tail is comprised mainly of particles inhabiting the “fringe” area in Fig. 3, our expectation is that the effect is a non-linear one. To investigate this further, we construct five restricted simulations and then attempt to predict their evolution using the diffusion formalism.

3.3 Initial setup for Gaussian radial action distributions

We set up five different Gaussian distributions in radial action and follow their evolution in a growing Keplerian potential. The black lines in Fig. 3 indicate the mean of the different distributions, highlight the respective values of 10, 50 and 200 $h^{-1} \text{kpc km s}^{-1}$. The solid black lines indicate two initial configurations in which we mostly confine the particles to the phase space area in which the evolution of the radial action is expected to be linear. The dotted lines indicate three simulations that are confined to the “linear” and the “transition” regimes. The simulation whose central value is 200 $h^{-1} \text{kpc km s}^{-1}$ is a special case, as here only a tiny part of the phase space is available which is entirely part of the “transition” area. This means that particles are confined to a very narrow area in phase space and that the average diffusion coefficient is rather large. As this implies that we are in close vicinity to the “fringe” of the potential, we do not expect that the evolution of this radial action distribution will be described well by the diffusion formalism. The parameters we have used to construct the initial conditions of the simulations are shown in table 1.

Fig. 4 shows a comparison of the initial coarse-grained distribution functions in $\mathcal{E} - J_r$ space between the “10-linear” case in the left panel and the “10-transition” case in the right panel. The Gaussian shape in the direction of J_r is apparent in both cases and reflects the input parameters given in Table 1. The distribution in energy is largely determined by the additional cuts we impose (see Table 1). In particular, the lower limit on the pericentre radius effectively introduces a new lower limit on the angular momentum. Hence, the largest values of \mathcal{E} which are theoretically available according to Fig. 3 are forbidden for particles with non-zero angular momentum. We find that in the “10-transition” case (right panel of Fig. 4), the “transition” area is populated whereas in the “10-linear” case it is not. This is a direct result of the energy cuts we imposed when sampling the initial distributions.

The distribution functions presented in Fig. 4 are calculated as a coarse-grained version of Eq. (29), which written as a function of both energy and angular momentum is

$$\begin{aligned} \tilde{N}_{i,j}(J_{r,i}, E_j) &= \sum_{k=0}^{N_{tot}} [\theta(\log(E_k) - \log(E_{j,min})) \\ &\times \theta(\log(E_{j,max}) - \log(E_k)) \theta(J_{r,k} - J_{r,i,min}) \\ &\times \theta(J_{r,i,max} - J_{r,k})]. \end{aligned} \quad (42)$$

Distribution	central J_r [h^{-1} kpc km s $^{-1}$]	σ_{J_r} [h^{-1} kpc km s $^{-1}$]	\mathcal{E}_{\min} [km s $^{-1}$]	$r_{\text{peri},\min}$ [h^{-1} kpc]	r_{ini} [h^{-1} kpc]	L_{ini} [h^{-1} kpc km s $^{-1}$]
10-transition	10	2	5.44	0.1	0.1-15	5-150
50-transition	50	3	3.32	-	0-15	5-150
200-transition	200	12	1.96	-	0-15	5-150
10-linear	10	2	20.06	0.1	0.1-15	2-50
50-linear	50	3	11.78	0.1	0.1-15	5-150

Table 1. The relevant parameters of the five particle distributions evolved in restricted N -body simulations are listed here. All distributions consist of 20000 particles which are initially sampled from a Gaussian distribution in radial action. “Linear” refers to distributions which are confined to the green area of Fig. 3 (i.e. the area in which the linear approximation of J_r is accurate). “Transition” refers to distributions which are confined to the green and cyan area, implying that the linear correction can be of the same order as the action itself for some particles. In column 2 we show the mean of the Gaussian distribution in each of the cases, whereas the spread of the distribution is given in column 3. The energy limit which is applied to confine the particles to the phase space areas specified above is shown in column 4. The last three columns show various additional cuts that have been imposed for numerical reasons. Column 5 shows minimum values for the pericenter radii, column 6 the range of initial radii at which we set up the tracers. The last column shows the initial range of angular momenta. Notice that in some cases, these collide with other cuts such as the pericenter radius cut. In fact, the reason for the “10-linear” cut to be different from the others is that with the imposed energy cut, no angular momenta larger than $50 h^{-1}$ kpc km s $^{-1}$ are allowed in the sampled range of radial actions.

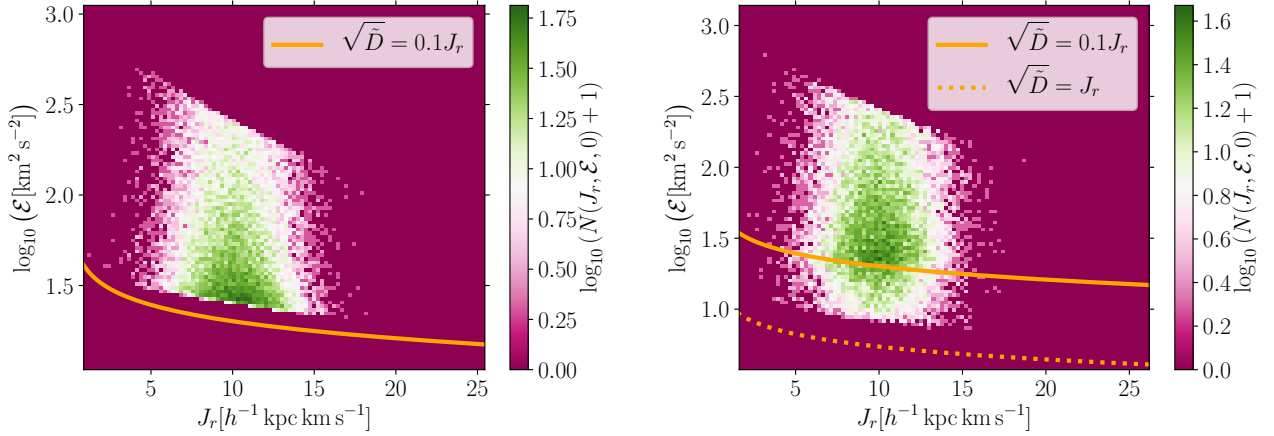


Figure 4. Comparison of the initial two-dimensional distribution functions in the 10-linear (left) and the 10-transition (right) cases. The lines defining the limits of the different regimes in Fig. 3 are shown as orange lines here. The solid orange line is the border between the “linear” and the “transition” regime, whereas the dashed orange line is the limit to the “fringe” regime. The logarithmic colour scale indicates the number of particles.

On the other hand, the coarse-grained versions of the drift and diffusion coefficients defined in Eqs. (38) and (39) are given by

$$\tilde{C}_{i,j}(J_{r,i}, E_j) = \frac{1}{N_{i,j}} \sum_{k=0}^{N_{tot}} \left| \begin{array}{l} J_{r,i,\min} < J_{r,k} < J_{r,i,\max} \\ E_{j,\min} < E_k < E_{j,\max} \end{array} \right. \left[-(\mathbf{r}_k \cdot \mathbf{v}_k) \frac{\dot{R}_k}{R_k} \frac{P(E_k)}{2\pi} \right] \quad (43)$$

$$\tilde{D}_{i,j}(J_{r,i}, E_j) = \frac{1}{2N_{i,j}} \sum_{k=0}^{N_{tot}} \left| \begin{array}{l} J_{r,i,\min} < J_{r,k} < J_{r,i,\max} \\ E_{j,\min} < E_k < E_{j,\max} \end{array} \right. \left[(\mathbf{r}_k \cdot \mathbf{v}_k) \frac{\dot{R}_k}{R_k} \frac{P(E_k)}{2\pi} \right]^2 \quad (44)$$

In Fig. 5 we show the coarse-grained drift and diffusion coefficients of the “10-transition” distribution in $\mathcal{E} - J_r$ phase

space at time $t = 0$. The drift coefficients (in units of h^{-1} kpc km s $^{-1}$) are shown in the left panel, while the diffusion coefficients (in units of $(h^{-1}$ kpc km s $^{-1})^2$) are shown on the right panel. Both the drift and the diffusion coefficients show the same trend with energy and radial action. The largest drift and diffusion coefficients are well within the “transition” area in phase space. Moreover, the largest drift coefficients are quite substantial in magnitude, up to the same order of magnitude as J_r itself. Furthermore, the average drift and diffusion coefficients rise with larger values of \mathcal{E} and J_r . Given that the largest drifts are found in the “transition” regime, which is not populated in the “10-linear” distribution (see Fig. 4), we expect that the diffusion formalism will lead to better results when applied to the “10-linear” case than when applied to the “10-transition” case.

Fig. 6 shows the initial diffusion coefficients in the 200-transition case. As expected from Fig. 3, the imposed con-

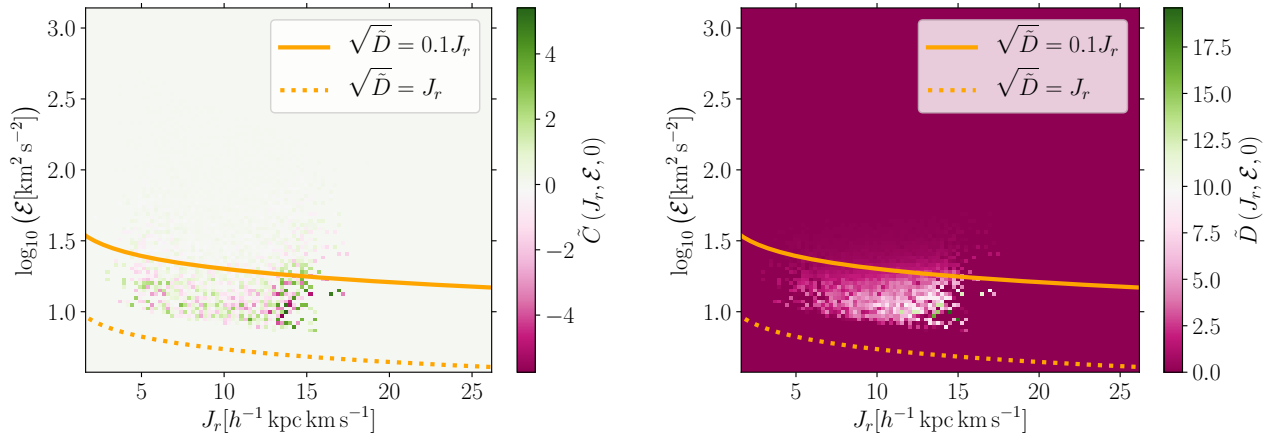


Figure 5. Initial drift (left) and diffusion (right) coefficients in the “10-transition” case as functions of energy and radial action. The colour scales indicate the drift/diffusion coefficient in units of $h^{-1}\text{kpc km s}^{-1}/(h^{-1}\text{kpc km s}^{-1})^2$ in the left/right panel. The orange lines are the same as in Fig. 4. Both the drift and diffusion coefficients rise in magnitude as energy and radial action increase. We find that in the “transition” area, the drift coefficients can reach values which are of the same order of magnitude as the radial action at which they are measured.

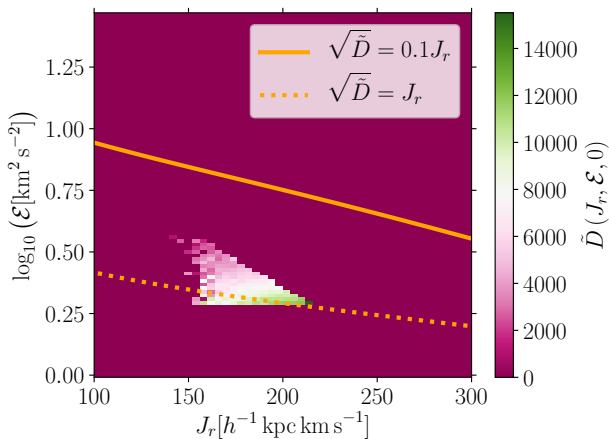


Figure 6. Coarse-grained diffusion coefficients for the “200-transition” distribution (see Table 1) at time $t = 0$ and in units of $(h^{-1}\text{kpc km s}^{-1})^2$. Only a narrow area in phase space is populated, which is very close to the border of the non-linear “fringe” regime in Fig. 3 (dotted orange curve here). The upper limit of the populated phase space area in the \mathcal{E} -direction is given by the $L = 0$ curve. We find that the measured diffusion coefficients are large over the entire populated phase space area, which reflects its closeness to the “fringe”.

dition that the “fringe” not be populated confines the particles to a rather small area in phase space. Since the populated phase space area lies in close vicinity to the “fringe”, the measured diffusion coefficients are very large. Given the magnitude of the averaged diffusion coefficients, we expect the evolution of the “200-transition” radial action distribution to be non-perturbative, and thus, it cannot be described by our diffusion formalism.

Overall, we expect the diffusion formalism to yield good results when applied to the evolution of the “10-linear” distri-

bution, while it should be clearly less accurate when applied to less linear areas in phase space, i.e. when analyzing the evolution of the “10-transition” and “50-transition” distributions.

4 TIME EVOLUTION OF RADIAL ACTION GAUSSIAN DISTRIBUTIONS IN A TIME-DEPENDENT KEPLERIAN POTENTIAL

In this section, we investigate the evolution of the five particle distributions introduced in Table 1. To this end, we transfer the diffusion formalism introduced in Peñarrubia (2015) to radial action space. We then investigate whether the evolution of the initial distributions is well described by first order drift and diffusion coefficients, calculated from the linear variation of Eq. (19). We find that while the evolution of some distributions is well captured by the diffusion formalism, the evolution of others is not, depending on which areas in phase space the original particle distributions occupy. Based on whether the diffusion formalism applies or not, we classify the evolution of radial action distributions as adiabatic or non-adiabatic. Finally, we investigate whether the net drift observed in Fig. 1 is an adiabatic or a non-adiabatic effect.

Similar to the discussion in Sections 3.1 and 3.2 of Peñarrubia (2015), we briefly discuss here how to obtain an invariant distribution $N(J_r, \rho)$ from the drift and diffusion coefficients and how to calculate $N(J_r, t)$ at a later time. Following the same arguments as in Section 3.1 of Peñarrubia (2015), and the same derivation that led us to Eq. (28), we find that the probability for a particle with action J_r at $t = t_0$ to have an

invariant action $J_{r'}$ is a Green function

$$p(J_{r'}|J_r, t_0) = \frac{1}{\sqrt{4\pi\tilde{D}(J_r, t_0)}} \times \exp\left\{-\frac{[J_{r'} - J_r - \tilde{C}(J_r, t_0)]^2}{4\tilde{D}(J_r, t_0)}\right\}. \quad (45)$$

The invariant distribution in radial action space can then be calculated from the radial action distribution at any time t_0 by performing the convolution

$$N(J_{r'}) = \int dJ_r p(J_{r'}|J_r, t_0) N(J_r, t_0). \quad (46)$$

Here $N(J_r, t_0)$ is obtained by marginalizing $N(E, J_r, t_0)$ over the energy. Knowing the drift and diffusion coefficients as a function of the invariant action throughout the simulation, we can use another convolution to calculate $N(J_{r'})$ at a later time.

Contrary to what happens to a particle's energy in a time-dependent potential, the time average of the radial action is constant according to Eq. (19), and thus we do not need an extra convolution analogous to Eq. 28 of Peñarrubia (2015). The radial action distribution at a time t is thus obtained from

$$N(J_r, t) = \int dJ_{r'} p(J_r, t|J_{r'}, t_0) N(J_{r'}), \quad (47)$$

with the probability function being the one defined in Eq. (28). In order to apply Eqs. (46) and (47) in a simulation, we marginalize the coarse-grained drift and diffusion coefficients defined in Eqs. (44) and (43) over the energy

$$\tilde{C}_i(J_{r,i}) = \frac{1}{N_i} \sum_{j=0}^{N_{bin}} \tilde{C}_{i,j}(J_{r,i}, E_j) \quad (48)$$

$$\tilde{D}_i(J_{r,i}) = \frac{1}{N_i} \sum_{j=0}^{N_{bin}} \tilde{D}_{i,j}(J_{r,i}, E_j), \quad (49)$$

where we have used

$$N_i = \sum_{j=0}^{N_{bin}} N_{i,j} \quad (50)$$

and N_{bin} is the number of bins in the energy dimension. In order to calculate $\tilde{C}(J_r', t)$ and $\tilde{D}(J_r', t)$, we calculate the invariant action J_r' for each particle, and then calculate the average drift and diffusion coefficients in equidistant bins in J_r' . Additionally, instead of using data obtained from the simulation itself, we can also assume that the particle distribution is phase-mixed. Under this assumption, $\tilde{C} = \partial\tilde{C}/\partial t = 0$ and the diffusion coefficient is given by Eq. (41).

4.1 The “10-linear” distribution and the role of the drift

In this section we apply the diffusion formalism to the “10-linear” case of Table 1. We calculate the required drift and diffusion coefficients in two different ways. First, we calculate them directly from the particle's orbital data using Eqs. (43) and (44). Then, by assuming the particle distribution to be phase-mixed, we set the drift coefficient to zero and calculate the diffusion coefficient using Eq. (41).

The upper panel of Fig. 7 shows the invariant distribution

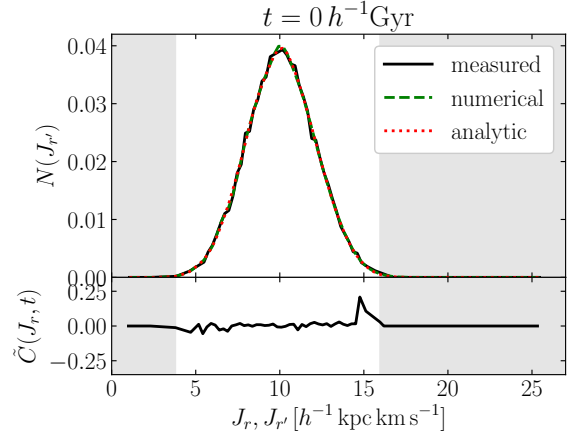


Figure 7. Invariant distribution $N(J_{r'})$ in the upper panel, and the drift coefficient $\tilde{C}(J_r, t)$ in the lower panel for the “10-linear” simulation at $t = 0$ (see Table 1). The black solid line is the measured distribution, obtained by calculating $J_{r'}$ for each particle and binning the results. The green dashed line is the result of the convolution (Eq. 46) using drift and diffusion coefficients obtained numerically from the data. The drift coefficient shown in the lower panel is the one depending on the instantaneous action J_r , i.e., the one that was used to do the convolution resulting in the green dashed line of the upper panel. The red dotted line in the upper panel shows the result of Eq. (46) using the analytic diffusion coefficient from Eq. (41). In order to avoid sampling noise in the data we combine bins with less than 50 particles in the tails of the distribution. In the grayed-in areas $\tilde{C}(J_r)$ is too poorly sampled.

$N(J_{r'})$ obtained at the start of the simulation in the “10-linear” case, while the lower panel shows the drift coefficient $\tilde{C}(J_r, t)$ that was used to calculate $N(J_r')$ using Eq. (46). To avoid a strong fluctuation in the drift coefficient in the tails of the distribution, we combine adjacent bins until the combined bin contains more than 50 particles. The center of the new bin is then calculated as a weighted mean of the centres of the combined bins, using the particle number as a weight. The grey area marks the radial action range in which the bins used to calculate the drift coefficients are empty after the re-binning procedure, suggesting that the drift obtained in this area is not a robust measurement due to insufficient particle sampling.

The result of the convolution in Eq. (46) using the coarse-grained coefficients is shown as a green dashed line in the upper part of Fig. 7, whereas the result obtained using the analytic diffusion coefficient from Eq. (41) is shown as a red dotted line. The “measured” distribution (black line) is obtained by calculating J_r' for each particle individually and then calculating a histogram in J_r' . Comparing the “measured” distribution with the calculated ones, we find that they all coincide remarkably well. This tells us that the assumption of phase mixing, i.e., $\langle \mathbf{r} \cdot \mathbf{v} \rangle = 0$ holds true, which comes as no surprise given the initial sampling algorithm was a rejection sampling with no preference for specific orbital branches. The measured drift coefficient $\tilde{C}(J_r, t)$ in the lower panel of Fig. 7 is further confirmation of the phase-mixing assumption holding true. We measure $\tilde{C}(J_r, 0) \approx 0$ over the entire relevant range of radial actions, with the exception of

one data point at the beginning of the tail of the distribution. For that reason, the analytic prediction, as well as the convolution based on particle data, provide a near perfect match to the measured distribution.

In Fig. 8 we show the distribution in radial action $N(J_r, t)$ at $t = 300 h^{-1} \text{Myr}$ in the left panel and at $t = 3 h^{-1} \text{Gyr}$ in the right panel. The colours used are the same as in Fig. 7. In the lower part of each panel we now show the drift coefficients dependent on the invariant action $\tilde{C}(J_r', t)$. With black solid lines we show the drift at the initial time, whereas blue dashed lines indicate the drift at the time at which the distributions are displayed in the top panels. As in Fig. 7, we combine bins with less than 50 particles using a weighted mean approach to determine the centre of the combined bin. As a result of this procedure, the drift measured at actions outside the range of populated bins is zero, and areas for which this is the case are coloured in grey.

Although at $t = 300 h^{-1} \text{Myr}$, $\tilde{C}(J_r', t)$ deviates strongly from zero at large radial actions, by $t = 3 h^{-1} \text{Gyr}$, it has decreased considerably over the entire range of invariant actions. The impact of this evolution in the drift is evident when comparing the “measured” distributions to the results of the “analytic” convolution. The former approach, which uses coarse-grained drift and diffusion coefficients measured from the particle distributions, provides a very good fit to the measured distribution at both times. The “analytic” approach, which uses the diffusion coefficient defined in Eq. 41 and no drift, yields a much better result in the right panel than in the left panel. Comparing $\tilde{C}(J_r')$ between panels, this is not surprising, since approximating the distribution as phase-mixed in J_r' is expected to work significantly better when $\tilde{C}(J_r')$ is indeed close to zero.

Overall, we conclude that the diffusion formalism outlined in Section 3 provides a remarkably good description of the time evolution of $N(J_r, t)$ in the “10-linear” simulation. In the next section, we will investigate if and how the accuracy of this formalism deteriorates when analyzing the evolution of the other distributions from Table 1.

4.2 Performance of the diffusion formalism

In this section we present results obtained when applying the diffusion formalism to the “10-transition”, “50-linear” and “50-transition” distributions from Table 1. For each of those cases, we show a comparison between the directly measured invariant distribution and the result of Eq. (46) at $t = 0$. We furthermore show a measurement of $N(J_r, t)$ after $3 h^{-1} \text{Gyr}$ of simulation time, as well as the result of the diffusion formalism using Eq. (47) and the initial radial action distribution $N(J_r, 0)$.

Fig. 9 shows the invariant distributions at time $t = 0$ in the “10-transition” (top), “50-linear” (middle) and “50-transition” (bottom) cases in the left column. In solid black lines, we show the “measured” distribution obtained by calculating the invariant action using Eq. (19) for each particle. The green dashed lines are the “convolved” distributions obtained from Eq. (46). We see that the match between the measured and the calculated distributions is quite accurate in the “10-transition” simulation (top left), and is only marginally worse in the “50-linear” case (mid left). However, in the “50-transition” case (bottom left), the agreement between the result of Eq. (46) and the direct measurement of $N(J_r')$ has de-

teriorated substantially compared to the other distributions. In particular, the result of the convolution is not able to resolve the peak in the measured invariant distribution and strongly over-predicts the occupancy of the tails.

The right column of Fig. 9 displays $N(J_r, t)$ after $3 h^{-1} \text{Gyr}$ in the “10-transition” (top), “50-linear” (middle) and “50-transition” (bottom) cases. Black solid lines are direct measurements, green dashed lines are the results of the convolutions (Eqs. 46 and 47) and red dotted lines show $N(J_r, t = 0)$ for comparison. The drift and diffusion coefficients are measured from the particle data following Eqs. (48) and (49).

In the “10-transition” simulation, shown in the top right panel of Fig. 9, we find a very good agreement between the measured distribution and the result of the diffusion formalism. Furthermore, we find that there is only relatively little evolution in the shape of $N(J_r, t)$ with the most obvious effect being the formation of a tail towards smaller values of J_r .

In the middle right panel, we show the “50-linear” distribution at the end of the simulation. Once more, we find a rather good agreement between the result of the diffusion formalism and the measured distribution, especially considering the rather strong evolution with respect to $N(J_r, 0)$. A slight mismatch can be observed in the tail of the distribution towards large values of J_r , where the convolution slightly overestimates the true measured distribution. Note that the diffusion formalism nonetheless provides a substantial improvement over the assumption that radial actions are invariant.

To explain why the evolution of the “10-transition” distribution appears to be better captured by the diffusion formalism than the “50-linear” distribution, we turn again to Fig. 3. While it is true that some particles in the “10-transition” case inhabit the cyan “transition” area, most particles are well within the “linear” regime (see right panel of Fig. 4). Furthermore, the linear energy range is much larger for $J_r = 10 h^{-1} \text{kpc km s}^{-1}$ than it is for $J_r = 50 h^{-1} \text{kpc km s}^{-1}$, i.e., in the former case particle orbits are more bound (shorter periods, see Eq. 20), and thus, the evolution of J_r becomes more and more adiabatic. Given that only a small fraction of particles inhabit the “transition” area in the “10-transition” case (relative to the large number of particles who inhabit more linear phase space areas than in the “50-linear” case), we conclude that on average its evolution is more adiabatic, and thus the diffusion formalism is more accurate, than that of the “50-linear” distribution.

In the bottom right panel of Fig. 9 we show the “50-transition” case. Fig. 3 suggests that the fraction of “transition” phase space area available to the particles is much larger here than in the “10-transition” case. Therefore, a substantial amount of particles in the “50-transition” simulation inhabit the “transition” area in phase space, i.e., the one bordering with the “fringe”. The consequences of this can already be seen in the mismatch between the measured and convolved invariant distributions in the bottom left panel of Fig. 9. In the bottom right panel, we find that $N(J_r, t)$ has evolved substantially at the end of the simulation, with an extended tail towards lower actions being present in the final distribution. While the peak of the distribution remains around its initial value of $50 h^{-1} \text{kpc km s}^{-1}$, its mean shifts towards smaller radial actions, causing the resulting distribution to deviate from Gaussianity. We find that the result of the dif-

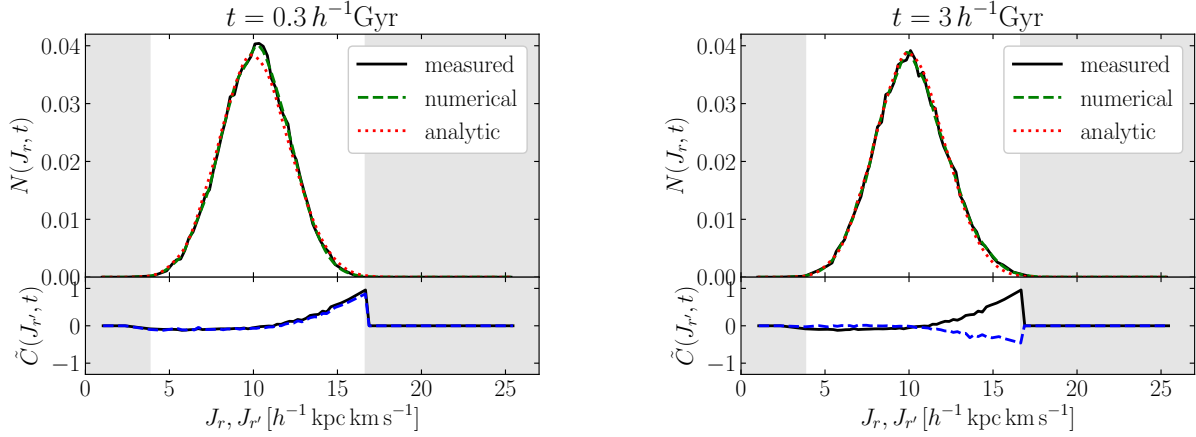


Figure 8. $N(J_r, t)$ at $t = 0.3 h^{-1} \text{Gyr}$ in the left panel and at $t = 3 h^{-1} \text{Gyr}$ in the right panel for the “10-linear” simulation (see Table 1). As in Fig. 7, the black line in the upper panels is the measured distribution, the green dashed line is obtained using the diffusion formalism with coefficients calculated from the simulation directly and the red dotted line is calculated using the analytic diffusion approach assuming phase mixing (no drift). In the lower panels, we show the drift coefficient used in the convolution (Eq. 47) to obtain the green dashed line in the upper panels. The black line in the lower panels is the drift coefficient $\tilde{C}(J_r, t)$ at $t = 0.$, whereas the blue dashed line is the one calculated at time t (shown in the upper legend). As in Fig. 7, we combine bins with less than 50 particles and the grey areas mark the range in which the drift coefficients lack particle sampling. Initially, the drift coefficient is non-zero, especially towards the tail of the distribution to the right, but it decreases considerably with time. In line with this, we find that the analytic approximation is not a perfect match at initial times, but improves significantly as phase mixing in $N(J_r)$ progresses.

fusion formalism does not fully capture the evolution of the radial action distribution. Most notably, it resolves neither the peak of the distribution nor the tail at large J_r values. This is to some extent expected, given that the calculated invariant distribution already deviates significantly from the measured invariant distribution (bottom left panel of Fig. 9). Interestingly, the tail of $N(J_r, t)$ towards smaller radial actions is captured quite well by the diffusion approximation, indicating that this is a linear effect. We note that the diffusion formalism still yields a considerable improvement over the assumption that $N(J_r, t)$ is invariant, yet the growing mismatch between the predictions of the formalism and the actual measurement is a strong hint that non-linear effects are becoming increasingly significant.

Finally, we note that the evolution of the “50-transition” distribution hints towards a drift towards smaller radial actions. Since this drift is roughly captured by the diffusion formalism, it appears to be an effect that is still almost adiabatic. Given that the number of particles around $J_r = 50 h^{-1} \text{kpc km s}^{-1}$ grows with time in Fig. 1, a much stronger drift towards smaller actions must occur at initially larger actions, where the available phase space becomes increasingly non-linear according to Fig. 3.

4.3 The “200-transition” distribution

According to Fig. 3, there is no “linear” phase space available for particles with $J_r = 200 h^{-1} \text{kpc km s}^{-1}$. We thus expect the evolution to be highly non-linear, despite confining the particles to the transition area initially. Indeed, we find that neither does the diffusion formalism manage to capture the evolution of $N(J_r, t)$, nor are we able to define the invariant distribution $N(J_r')$ using Eq. (46). Instead, we find that the “invariant” distribution we measure using Eq. (19) exhibits

a strong evolution with time. To understand this better, we look at the time evolution of both $N(J_r, t)$ and $N(J_r')$, where J_r' is defined by Eq. (19) and cannot be considered a dynamical invariant.

Fig. 10 shows the time evolution of both $N(J_r, t)$ (in the lower panel) and $N(J_r')$ as calculated using the linear approximation (Eq. 19) in the upper panel. We see a strong time evolution in the latter. The fact that $N(J_r')$ is not time-invariant indicates that the evolution of the “200-transition” distribution is highly non-adiabatic (and clearly non-linear). However, the evolution of the “invariant” distribution explains some of the time evolution of $N(J_r, t)$ in the bottom panel of Fig. 10. While $N(J_r, t)$ is initially a Gaussian distribution set up as in Table 1, the initial “invariant” distribution is bimodal, with one peak around $50 h^{-1} \text{kpc km s}^{-1}$ and a second peak around $350 h^{-1} \text{kpc km s}^{-1}$.

This initial bimodal shape of the distribution can be explained by Fig. 6. A large fraction of the particles in the “200-transition” distribution populates a phase space region with diffusion coefficients of the order of J_r^2 . This implies that for most individual particles, the linear variation is of the order of the central radial action itself. Since its sign depends on the direction of the particle’s radial velocity, the linear correction can be either positive or negative. Therefore, particles with $J_r = 200 h^{-1} \text{kpc km s}^{-1}$ can have a linear invariant action which is either larger or smaller by an amount roughly equal to J_r itself. This implies that the diffusion formalism breaks and we can only qualitatively explain the evolution of the radial action distribution.

We find that right after the start of the simulation, $N(J_r, t)$ develops a bimodal structure. This can be explained by phase mixing separating the particles belonging to different peaks of the “invariant” distribution (black solid line in the upper panel of Fig. 10). To try to explain the evolution beyond

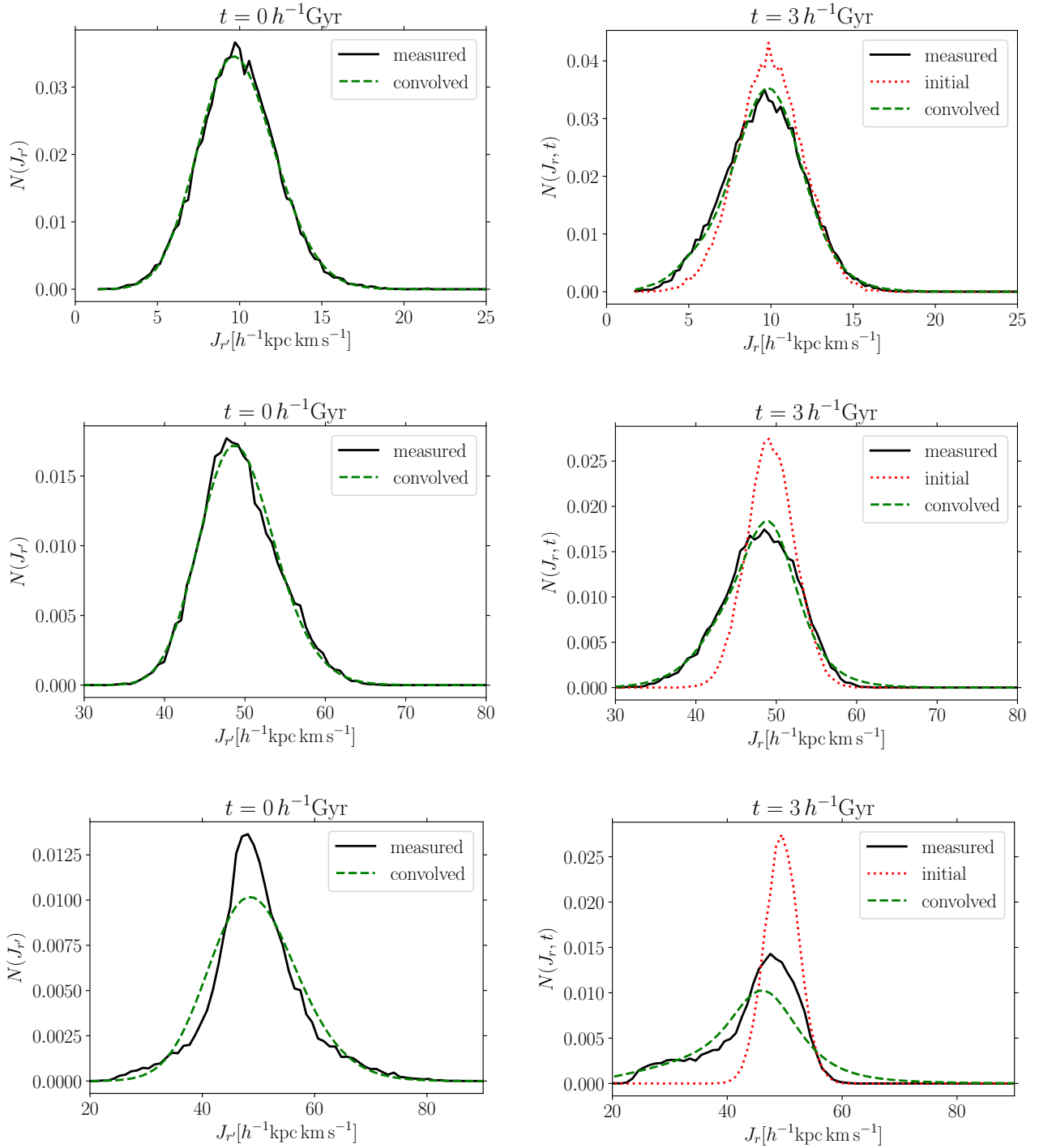


Figure 9. Invariant distributions (on the left) and radial action distributions after a simulation time of $3 h^{-1} \text{Gyr}$ (on the right) of the “10-transition” simulation (top row), the “50-linear” simulation (middle row) and the “50-transition” simulation (bottom row); see Table 1. The green dashed lines marked “convolved” are the result of applying the diffusion formalism (Eqs. 46 and 47) using coarse-grained drift- and diffusion coefficients (see Eqs. 48 and 49). The black lines marked “measured” are direct measurements of the distributions. In the right panels, we also show $N(J_r, t = 0)$ as red dotted lines.

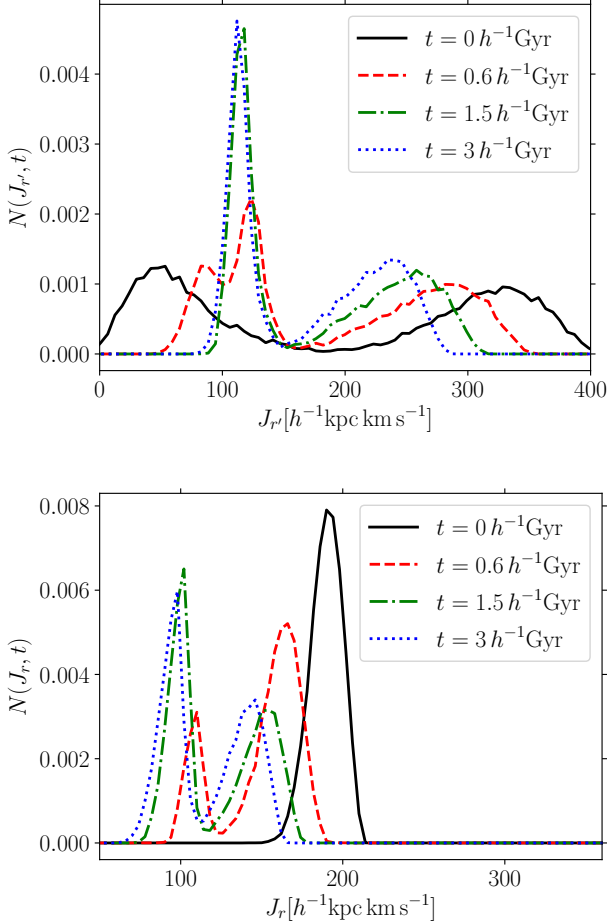


Figure 10. Time evolution of $N(J'_r)$ as defined in Eq. (19) (upper panel) and of $N(J_r, t)$ (lower panel) for the “200-transition” case (see Table 1). Different lines correspond to distributions at different times as described in the legends.

that, we calculate $N(J'_r)$ at various times keeping the second order terms of Eq. (17) (see Appendix B for the detailed calculation). This is shown in Fig. 11 where J'_r is now defined by Eq. B19. Initially, the second order version of $N(J'_r, t)$ is clearly more populated around $J'_r = 200 h^{-1} \text{kpc km s}^{-1}$ than the first order (linear) version shown on the upper panel of Fig. 10. The bimodal shape of the linear version of $N(J'_r)$ vanishes when including second order corrections. Instead, the second order $N(J'_r)$ now obtains an extended tail at large values of J'_r , which demonstrates that higher order corrections are rather significant for the “200-transition” distribution.

Both $N(J_r, t)$ and the second order version of $N(J'_r)$ exhibit a net drift towards smaller radial action values over the course of the simulation. As the second order “invariant” distribution is still not a true invariant, we conclude that the evolution of the “200-transition” distribution is truly non-linear and non-adiabatic. To explain the slow drift towards smaller radial actions, we recall that the time-dependent energy of a particle, as defined in Eq. (B1) (at second order), depends strongly on the particle’s phase space coordinates. In particular, particles inhabiting the “fringe” of the potential can have

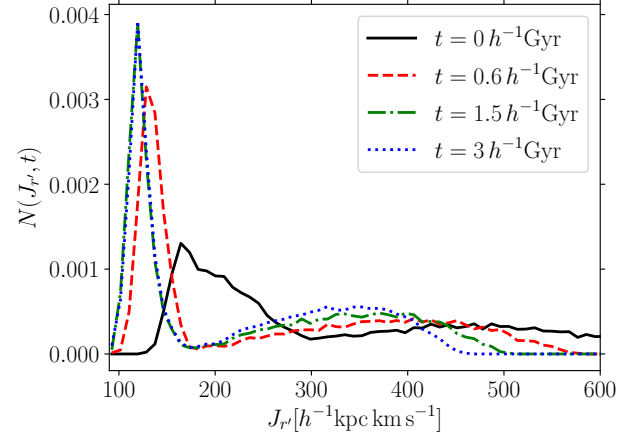


Figure 11. Time evolution of the “invariant” distribution for the “200-transition” case (see Table 1) calculated using a second order expansion of the radial action (Eq. B19). Different lines correspond to distributions at different times as given in the legend.

very large energies on a small part of their orbits and smaller energies over the rest of their phase space trajectory. Hence, as the radial action is given by Eq. (3) in a Keplerian potential, these particles can have large instantaneous actions for a small fraction of their orbit and then slowly drift towards smaller actions for the rest of the orbital time. As the orbital times are very long for particles with large energies, this drift occurs very slowly. Furthermore, since the orbital times of individual particles in the “fringe” of the Keplerian potential used in the “200-transition” simulation can exceed the age of the Universe, the initial radial action distribution will never be restored. Therefore, we conclude that the evolution of the “200-transition” distribution is fully non-adiabatic and the drift observed in Fig. 1 is a non-linear effect which can not be captured by the diffusion formalism developed in Section 3.

5 A COUPLE OF CONSEQUENCES FOR DARK MATTER HALOES

So far, our discussion has been focused on the evolution of radial action distributions in a Keplerian host potential. While it is possible to develop a diffusion formalism that accurately describes the time-evolution of radial action distributions in a large part of phase space, we have found that in the “fringe” of the potential, i.e., at large (nearly unbound) orbital energies, the evolution is non-adiabatic and the diffusion formalism breaks down. Hereafter, we discuss a couple of examples where the diffusion formalism developed in Section 3, and its limitations (i.e. non-adiabaticity), provide new physical insights. These examples are i) the mass accretion history of a Milky-Way (MW) like halo and ii) core formation in a self-interacting dark matter (SIDM) halo. For both of these cases, we discuss whether or not the rate of change of the self-gravitating potential of the halo implies an adiabatic evolution of the radial action distributions of tracers.

5.1 Mass accretion in dark matter haloes

Pontzen & Governato (2013) attempted to explain the shape of dark matter haloes using a maximum entropy approach with the additional assumption that radial actions are conserved. The authors found that a single population of particles is, under these assumptions, not sufficient in order to explain the shape of DM haloes from first principles.

In this section, we apply the formalism presented in Sections 3 and 4 to assess whether, under the assumption of spherical symmetry, radial actions truly evolve adiabatically (and are thus approximately conserved) during the assembly of an idealised Milky-Way (MW) size DM halo. Specifically, we self-consistently construct an idealised MW-size halo following a Hernquist density profile at two different redshifts. To do this, we use the mean accretion history reported in Boylan-Kolchin et al. (2010) to determine the mass of the halo at a given redshift and use the rejection sampling scheme described in Burger & Zavala (2019) based on Eddington's formalism (Eddington 1916, Binney & Tremaine 1987) to sample a particle representation of the DM halo in dynamical equilibrium. We then calculate the diffusion coefficient of each individual DM (simulation/sampled) particle from Eq. (39). The MW-like halo we consider here has a virial mass of $M_{200} = 10^{12} h^{-1} M_{\odot}$ and a concentration¹ of $c_{200} = r_{200}/r_{-2} = 12$ at redshift $z = 0$. These are typical values for MW-like haloes (e.g. Boylan-Kolchin et al. 2010). For the scale factor $R(t)$ (formally given by Eq. 8), we use an approximate formula derived in analogy to the scale-free case (Eq. 37)²:

$$R(t) = \frac{1}{2 + \alpha(r, t)} \left(\frac{\Psi(r, t)}{\Psi(r, 0)} \right)^{-\frac{1}{2 + \alpha(r, t)}}, \quad (51)$$

where

$$\alpha(r, t) = \frac{d \log(\Psi(r, t))}{d \log(r)} \quad (52)$$

is the logarithmic slope of the potential at a given radius and

$$\Psi(r, t) = \Phi(r, t) - \Phi(0, t) \quad (53)$$

is the potential shifted such that $\Psi(0, t) = 0$. To calculate the diffusion coefficient, we need the time derivative of the scale factor, namely

$$\frac{dR}{dt} = -\frac{1}{(2 + \alpha(r, t))^2} \times \left(\frac{\Psi(r, t)}{\Psi_0(r)} \right)^{-\frac{1}{2 + \alpha(r, t)}} \times \left\{ \left[1 - \frac{1}{2 + \alpha(r, t)} \ln \left(\frac{\Psi(r, t)}{\Psi_0(r)} \right) \right] \times \frac{d\alpha}{dt} + \frac{\dot{\Psi}}{\Psi} \right\}. \quad (54)$$

In our model scenario of mass accretion into a MW-size halo, we assume that mass accretes primarily into the outer parts of the halo, leaving the inner mass content unchanged. This is in line with the simple picture of cosmological halo mass assembly in layers/shells in which the concentration parameter $c_{200} = r_{200}/r_{-2}$ evolves with redshift only due to the

¹ With r_{-2} being the radius at which the logarithmic slope of the halo's density profile equals -2 and r_{200} the radius at which the enclosed density equals 200 times the critical density of the Universe.

² For a discussion of the validity of this approximation see Appendix C)

evolution of $r_{200} \propto (1 + z)$ in an expanding Universe. This simple picture is approximately validated by full cosmological N -body simulations (e.g. Sánchez-Conde & Prada 2014, Ludlow et al. 2014). Under these assumptions, the scale radius in a Hernquist halo can be written as a function of redshift as

$$r_s(z) = 2r_{-2}(z) = \frac{2(1 + z)}{c_{200,0}} \left(\frac{GM(z)}{100H^2(z)} \right)^{1/3}, \quad (55)$$

where $c_{200,0}$ is the concentration parameter at the current time, $M(z)$ is the redshift-dependent halo mass and $H(z)$ is the Hubble rate. In a Hernquist halo,

$$\alpha(r, z) = 1 - \frac{r}{r + r_s(z)} \quad (56)$$

$$\Psi(r, z) = \frac{GM(z)r}{r_s(z)(r + r_s(z))} \quad (57)$$

and we can thus write the relevant time derivatives in equation 54 as

$$\frac{\dot{\Psi}}{\Psi} = \frac{\dot{M}}{M} - \frac{r + 2r_s}{r_s(r + r_s)} \dot{r}_s \quad (58)$$

$$\frac{d\alpha}{dt} = \frac{r}{(r + r_s)^2} \dot{r}_s, \quad (59)$$

where we suppress the redshift-dependence and derivatives are taken with respect to cosmic time. In our model of mass accretion, the density profile is that of a Hernquist halo at all redshifts. Therefore, for most times and radii, we expect that the evolution of the potential's logarithmic slope is negligible. For the cases we study in the following, we have explicitly verified that $\dot{\Psi}/\Psi \gg \dot{\alpha}$. Independent of our definition of the static frame in which we define the action invariant, and hence independent of the definition of $\Psi_0(r)$, we therefore find that

$$\frac{\dot{R}}{R} = -\frac{1}{2 + \alpha(r)} \left(\frac{\dot{M}}{M} - \frac{r + 2r_s}{r_s(r + r_s)} \dot{r}_s \right). \quad (60)$$

In order to evaluate Eq. (60) at different times, we adapt the median mass accretion history for MW-like haloes reported in Boylan-Kolchin et al. (2010)

$$M(z) = M_0 (1 + z)^\eta \exp(-\kappa'(\sqrt{1 + z} - 1)), \quad (61)$$

with $\kappa' = 4.9$ and $\eta = 2.23$. Thus

$$\frac{\dot{M}}{M} = \left(\frac{\eta}{1 + z} - \frac{\kappa'}{2\sqrt{1 + z}} \right) \times \frac{dz}{dt} \quad (62)$$

$$= \left(\frac{\eta}{1 + z} - \frac{\kappa'}{2\sqrt{1 + z}} \right) \times (-(1 + z)H(z)) \quad (63)$$

where $H(z)$ is the Hubble rate at redshift z . At the current time ($z = 0$) we find that for $M(z = 0) = 10^{12} h^{-1} M_{\odot}$ and $c_{200,0} = 12$,

$$\frac{\dot{M}}{M}(z = 0) \approx 2.24 \times 10^{-2} h \text{ Gyr}^{-1}. \quad (64)$$

In the past, however, the amplitude of the specific accretion rate may have been very different. As an example, let us look at the redshift maximizing $dM/dz/M$, which is easily shown to be

$$1 + z_{\max} = \frac{16\eta^2}{\kappa'^2}. \quad (65)$$

At this redshift, we find that $M(z = z_{\max}) \approx 2.6 \times$

$10^{11} h^{-1} M_{\odot}$ and

$$\frac{\dot{M}}{M}(z = z_{\max}) \approx 0.5 h \text{ Gyr}^{-1}. \quad (66)$$

The second term in equation 60 can be written as

$$\dot{r}_s = -(1+z)H(z)\frac{dr_s}{dz}. \quad (67)$$

Throughout our calculations, we use $\Omega_{\Lambda,0} = 0.7$ and $\Omega_{m,0} = 0.3$. Using Eq. (60), we can now calculate the theoretical diffusion coefficients at different redshifts using Eq. (41). To that end, we calculate energy, angular momentum, radius and radial velocity of each (simulation) particle in our halo. We then numerically calculate the radial action and the radial period of each particle, as well as the integral C7 in Peñarrubia (2019), which is related to the expectation value of the squared radial velocity needed to evaluate Eq. (41). From the ratio $\sqrt{\bar{D}}/J_r$ we then construct the “linear”, “transition” and “fringe” areas introduced for the Keplerian potential in Fig. 3 for the case of mass accretion onto a DM halo.

Fig. 12 shows the phase space distribution of one million particles at different times. In the upper panel, we show the distribution at the redshift z_{\max} at which the specific accretion rate peaks. The lower panel displays the phase space distribution today. In each panel, we show the fraction of particles inhabiting the different phase space regions, which correspond to the ones introduced in Fig. 3 for the time-dependent Keplerian potential. The boundaries between the different regions are obtained by sorting the particles within different radial action bins by their respective values of $\sqrt{\bar{D}}/J_r$.

In the upper panel of Fig. 12, we see that at $z = z_{\max}$ only $\sim 41\%$ of the particles in the DM halo inhabit the “linear” phase space area in which the diffusion formalism applies, while $\sim 18\%$ are located in the “fringe”, where we expect highly non-linear evolution. Just as in the Keplerian case, at large values of J_r , we find that the phase space area of the “linear” regime shrinks and eventually disappears with all particles at very large radial actions being in the “fringe”, where the evolution of the radial action is non-linear. We note that in the Keplerian case, particles with these large actions tend to drift towards smaller values of J_r on short to intermediate time-scales. Since such drift does not seem to occur in the opposite direction in the Keplerian case, i.e., particles tend to maintain small values J_r over a comparatively long time (see Fig. 2), radial actions which are too large to satisfy a “linear” evolution are effectively erased from the distribution. Assuming that this quantitative behaviour will be the same in a DM halo (with a potential closer to that of a NFW distribution) a phase space distribution of DM particles such as the one seen at $z = z_{\max}$ could have significant consequences. In particular, if the “fringe” is as populated as in the upper panel of Fig. 12, the radial action distribution is expected to be skewed towards smaller radial action at later times, i.e., the amount of particles with smaller radial actions increases and the tail of the distribution is erased. In principle, this is a temporary effect for individual particles. However, as the radial period sets the relevant time-scale, and orbits in the fringe have large periods, it takes some time to restore each individual action to its initial value. Moreover, since the orbital times of different particles are not exactly the same, the full initial distribution is never restored.

The lower panel of Fig. 12 shows the phase space occupancy

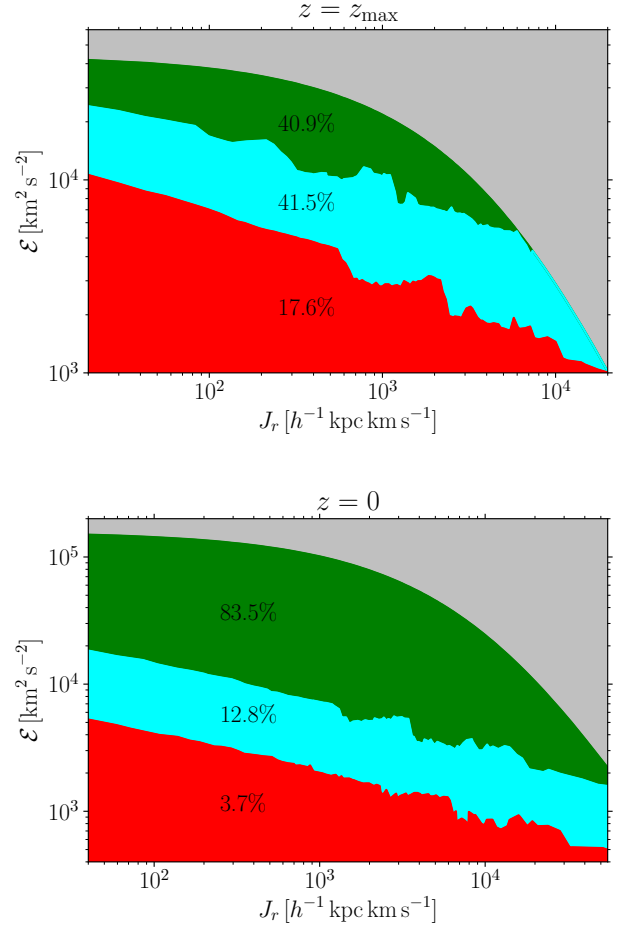


Figure 12. Occupation of the $\mathcal{E} - J_r$ phase space in an idealised MW-size halo accreting mass according to the mass assembly history obtained in cosmological simulations (see Eq. 63). The silver area is not populated, the green area is the “linear” regime in which $\sqrt{\bar{D}}/J_r < 0.1$. The area coloured in cyan is the “transition” area in which $\sqrt{\bar{D}}/J_r < 1$ and the red area is the “fringe” of the potential. The fraction of particles in the different regions is shown as a percentage of the total amount of particles. The upper panel shows the phase space occupancy at $z = z_{\max}$, the redshift at which the specific accretion rate is maximal, whereas the lower panel displays the phase space occupancy at $z = 0$.

today. In contrast to the upper panel, the evolution of radial actions in a MW-size halo today is on average significantly more adiabatic, with 83 per cent of particles inhabiting the “linear” regime, as opposed to only 3.7 per cent that inhabit the “fringe”. This implies that *at the current time*, it is a fair approximation to assume that radial actions are conserved in a MW-size halo.

In conclusion, we state that when attempting to explain the shape of the dark matter halo density profile from first principles, as was done in e.g. Pontzen & Governato (2013), it is important to take into account the fact that, even under the assumption of spherical symmetry, radial actions have not been constant throughout the accretion history of the halo. As a consequence of this, the assembly process of a DM halo is likely to leave an imprint in the radial action

distribution. We thus deem it plausible that the accretion history of DM haloes is connected to the eventual shape of the halo via mutual feedback. While the impact of a large mass accretion depends on the shape of the halo when accretion occurs, orbits of individual particles change in response to the accretion, which in turn alters the halo shape.

In order to investigate this more rigorously, one needs to repeat the analysis presented here on full cosmological simulations, since it is crucial to trace the evolution of the radial action distribution without dictating a parametric halo density profile. In this way, the interplay between the radial action distribution and the halo density profile can be observed at different accretion rates. To take triaxiality into account, it is possible to perform the above analysis on integrals of motion derived in coordinate systems with a triaxial symmetry.

If we can accurately model the interdependence between the evolution of radial actions of particles in the MW and the MW’s accretion history, it may be possible to use our diffusion algorithm to improve the analysis of tidal streams in the MW. [Buist & Helmi \(2015\)](#) have analyzed the evolution of radial action distributions of tidal streams in a time-dependent Aquarius potential. In tidal streams whose orbits are not adiabatic, they find an increased spread in radial action between the stream particles when compared to the final distribution in a static potential. Our results suggest that this additional spread can be modelled as the result of a diffusion process in radial action space. Furthermore, this diffusion in radial action space constitutes an additional error source when using the clustering of tidal streams in action space to constrain the potential of the Galaxy, as was done, e.g. by [Sanderson et al. 2015](#) and [Sanderson et al. \(2017\)](#). In particular, our results suggest that the accuracy of the assumption that the true potential implies the most tightly clustered radial action distribution depends on both the accretion history of the MW and the orbit of the tidal stream’s progenitor.

5.2 Cusp-core transformation in SIDM

[Burger & Zavala \(2019\)](#) looked at the evolution of a set of tracer particles with a Gaussian distribution in radial action orbiting in the potential of a dwarf-sized DM halo developing a constant density core in one of two different ways³. One way of forming a core was through elastic self-scattering between the DM particles (SIDM). Another way of forming a constant density core was through impulsive energy injections into the system in a way akin to supernova feedback. Fig. 7 in [Burger & Zavala \(2019\)](#) shows a comparison of the final radial action distributions of the tracer particles in these two reference scenarios, as well as a third baseline scenario in which the host halo retains its cusp. From this figure, it is clear that $N(J_r, t)$ at the end of the SIDM simulation, which has a cusp-core transformation, is very close to the final distribution in the benchmark simulation (without a cusp-core transformation). It appears that the difference between those two distributions can be explained by diffusion in radial action space. Hence, we expect that a large part of the $\mathcal{E} - J_r$ phase space area

occupied by particles orbiting in a SIDM halo belongs to the “linear” regime of radial action evolution.

To test this hypothesis, we calculate the diffusion coefficients of all the DM particles in a SIDM halo similar to the one used in [Burger & Zavala \(2019\)](#) following Eq. (39). The only difference is that we re-run the SIDM simulation with a smaller self-interaction cross section of $\sigma/m_\chi = 1\text{cm}^2\text{g}^{-1}$. Furthermore, we now save snapshots (simulation outputs) every $0.1 h^{-1}\text{Gyr}$ and calculate the potential $\Psi(r)$ by averaging the potential of tracer particles in logarithmically spaced spherical shells. As we require the function $\Psi(r, t)$ in order to calculate the approximate value of the scale factor (Eq. 51) and its time derivative, we calculate $\Psi(r)$ at each snapshot and then interpolate between snapshots.

The scale factor itself is calculated following Eq. (51) at a fixed time. As $\alpha(r, t)$ can not be calculated analytically, we evaluate it numerically by interpolating the function $\log(\Psi(\log(r)))$ and calculating its derivative at each (simulation) particle’s radius. Moreover, as the time-dependence of $\alpha(r, t)$ is now significant, the derivative of the scale factor at a given radius is now given by Eq. (54), where the terms proportional to $d\alpha/dt$ are sizeable and can thus not be neglected. In order to calculate $\dot{\alpha}$ and $\dot{\Psi}$, we first identify each DM particle’s radius and then calculate $\alpha(r, t)$ and $\Psi(r, t)$ as functions of time at the particle’s radius. The time derivatives are calculated numerically from the interpolated functions. We finally proceed to calculate $\tilde{D}(J_r, \mathcal{E})$ from Eq. (41) in the same way we did in Section 5.1, but using $\Phi(r, t)$ of the SIDM halo when calculating J_r , P and integral C7 of [Peñarrubia \(2019\)](#).

Several stages during the process of core formation in a SIDM halo are interesting to analyze. Initially, the central density of the DM halo decreases rapidly forming an inner cored profile, followed by a phase during which full thermalization occurs. In the latter, due to the mass redistribution, the central density is completely flat (isothermal core) in the centre followed by a small region outside the inner core (but still within the scale radius) where the density rises slightly above that of the original profile (see e.g. [Vogelsberger et al. \(2012, 2014\)](#)). Over the course of our simulation, the halo whose evolution we follow passes through the first stage and is in the middle of the second stage as the simulation ends, indicating that a cross section of $\sigma/m_\chi = 1\text{cm}^2\text{g}^{-1}$ is not sufficient to produce a fully thermalized core in a dwarf-sized DM halo in a time of $3h^{-1}\text{Gyr}$. Notably, including baryons into the simulation can change this picture (see [Santos-Santos et al. \(2020\)](#) or [Robles et al. \(2017\)](#)). Furthermore, we briefly note that there is an additional phase for large SIDM cross sections called gravothermal collapse (e.g. [Zavala et al. \(2019\)](#) and [Turner et al. \(2020\)](#)) in which the core collapses to very large densities. Since our self-interaction cross section is too small for this process to occur, we do not discuss it here.

Fig. 13 shows the evolution of the central part of the SIDM-halo’s density profile in our simulation. The black solid line is the initial density profile. In dashed orange we show the density profile after $0.3 h^{-1}\text{Gyr}$ and the red dashed line is the density profile after $2.7 h^{-1}\text{Gyr}$. Blue lines denote snapshots between and or after the ones highlighted in the legend. The grey shaded area shows the resolution limit for CDM simulations, the so-called “Power radius” ([Power et al. \(2003\)](#)). We note that SIDM profiles are usually converged to well within the Power radius ([Vogelsberger et al. 2012](#); [Rocha et al. 2013](#);

³ The halo used was a dwarf-sized halo which initially has a Hernquist density profile with mass $M_{200} = 10^{10} h^{-1} M_\odot$; see Table 1 of [Burger & Zavala \(2019\)](#) for the relevant simulation parameters.

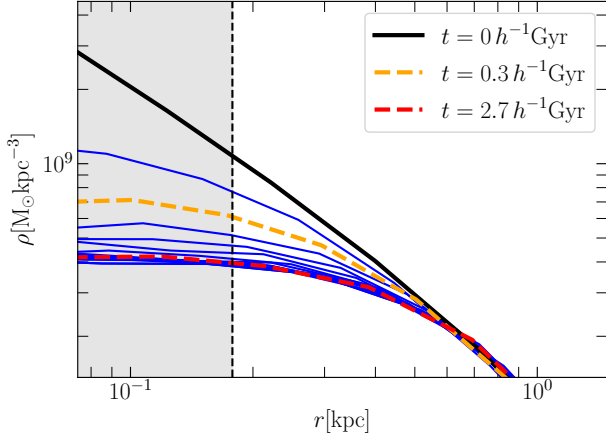


Figure 13. Evolution of the density profile in the inner region of a dwarf-size SIDM halo with $\sigma/m_\chi = 1\text{cm}^2\text{g}^{-1}$. Lines denote the halo density profile at different times. The black solid line marks the density profile at the beginning of the simulation, whereas the orange and red dashed lines are the density profiles after $0.3h^{-1}\text{Gyr}$ and $2.7h^{-1}\text{Gyr}$ of simulation time respectively. Blue lines indicate the evolution in between other snapshots. The gray shaded area denotes the resolution limit of the equivalent CDM-only simulation (see [Burger & Zavala 2019](#)).

[Vogelsberger et al. 2014](#)). It is apparent that the orange line illustrates the first part of the core formation process, the rapid decrease in mass density in the innermost part of the halo. The red line, on the other hand, is part of the more slowly occurring phase in which the density in the immediate surroundings of the central core rises and the core fully thermalizes. We have chosen those two times because they represent different stages of the core formation process in a SIDM halo.

Fig. 14 shows the phase space plots for the SIDM halo at the times corresponding to the orange dashed line ($0.3h^{-1}\text{Gyr}$) and the red dashed line ($2.7h^{-1}\text{Gyr}$) in Fig. 13. The areas in the plot correspond to the equivalent areas in Fig. 12. Evidently, the change in gravitational potential due to core formation (induced by DM self-interactions) causes a mostly adiabatic evolution of radial action distributions over the entire simulation time. In both panels of Fig. 14, more than 97 per cent of DM particles are in the “linear” phase space area and only around 1 per cent inhabit the “fringe”. As a consequence, we expect the radial action distribution of tracer particles to be altered very little, if at all, by the change in gravitational potential triggered by SIDM, provided that the self-interaction cross section remains within an amplitude that is allowed by astrophysical constraints.

We remark that the statement that the evolution of radial action distributions in an SIDM halo is expected to be linear and can be described by our diffusion formalism applies only to kinematic tracers. For the DM particles themselves, SIDM-induced elastic collisions are a different matter as the radial action of both collision partners changes in a random fashion, since their post-collision orbits are entirely different from the pre-collision orbits. When we talk about an “adiabatic” or “linear” response of a radial action distribution, we

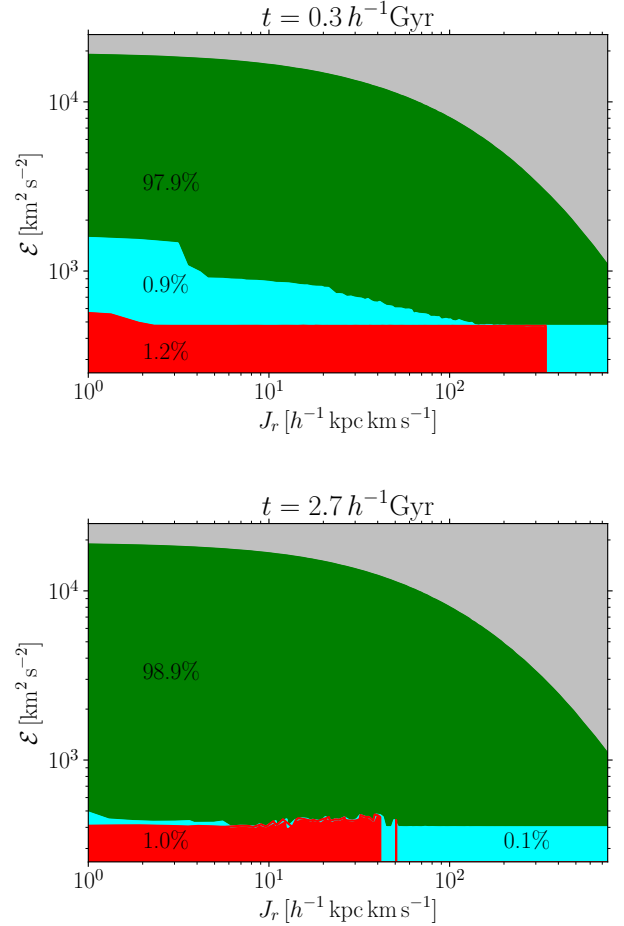


Figure 14. The $\mathcal{E} - J_r$ phase space and how it is populated in a dwarf-size halo forming a core due to self-scattering between its DM particles. The different curves and areas are equivalent to those in Fig. 12. The fraction of DM particles populating each area of phase space is shown as a percentage in the respective areas. The upper panel corresponds to the orange dashed line in Fig. 13 (early-stage in core formation), while the lower panel corresponds to the red dashed line in Fig. 13 (late-stage in core formation).

are strictly speaking of particles which are not subjects to discrete collisions themselves.

We apply the diffusion formalism presented in Sections 3 and 4 to describe the evolution of a Gaussian radial action distribution comprised of 20000⁴ tracer particles orbiting in the core-forming SIDM halo. Since we cannot calculate exact orbit-dependent values of $R(t)$ for tracer particles in an SIDM halo, we have to use the approximations given by Eqs. (51) and (54) to obtain the drift and diffusion coefficients. In Appendix C, we demonstrate that the evolution of radial actions of kinematic tracers in a potential with a time-dependent shape is accurately described by this approximate scale factor. Since the rate at which the shape of the potential in

⁴ To enable us to derive smoother drift and diffusion coefficients, we have added 18000 tracers to the original 2000 used in [Burger & Zavala \(2019\)](#). They are set up in exactly the same way as the initial 2000 tracers and thus obey the same Gaussian distribution.

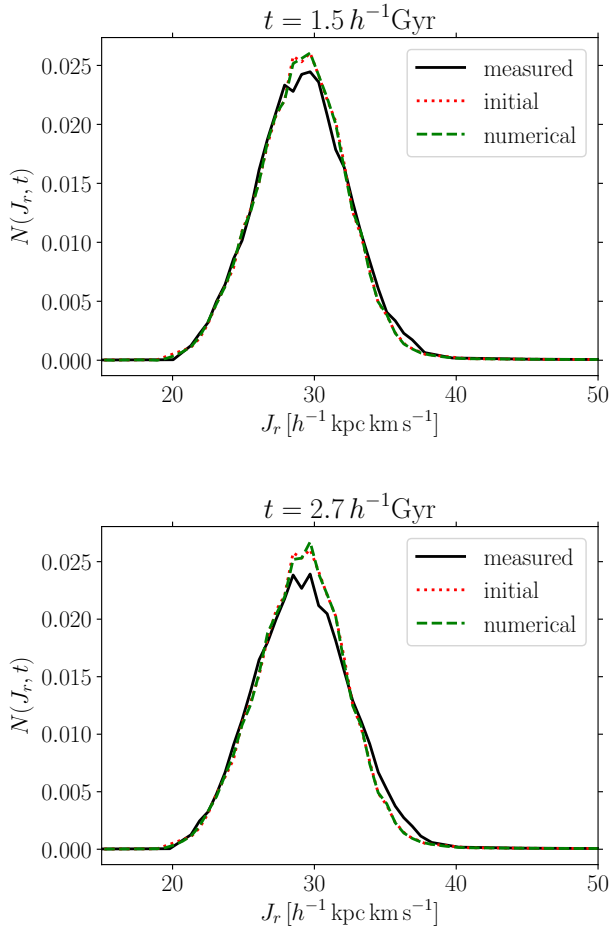


Figure 15. Radial action distribution of 20000 tracer particles after $1.5 h^{-1}\text{Gyr}$ of simulation time (top panel) and after $2.7 h^{-1}\text{Gyr}$ of simulation time (bottom panel) in the core-forming SIDM halo shown in Fig. 13. The black lines show the measured distribution. The red dotted line is the initial distribution and the green dashed line denotes the result of the diffusion formalism.

Appendix C changes is larger than the rate at which the potential of the SIDM halo changes, we conclude that we can use Eqs. (51) and (54) to obtain accurate predictions of the evolution of $N(J_r, t)$ in a core-forming SIDM halo.

Fig. 15 shows the “measured” radial action distribution (black solid line) after $1.5 h^{-1}\text{Gyr}$ of simulation time in the top panel and after $2.7 h^{-1}\text{Gyr}$ in the bottom panel, along with the result of the diffusion formalism (green dashed line) and the initial distribution (red dotted line). Since the calculation of the drift and diffusion coefficients involves numerical derivatives of time-dependent measured quantities, we take $N(J_r, t)$ at $t = 0.3 h^{-1}\text{Gyr}$ as the initial distribution in order to assure that the time-derivatives are numerically stable. We find that the prediction from the diffusion formalism is overall in good agreement with the measured distribution in Fig. 15 (particularly in the early stages of core formation; see upper panel). However, in the late stage of core formation (between $1.5 h^{-1}\text{Gyr}$ and $2.7 h^{-1}\text{Gyr}$) the measured distribution gradually forms a slightly more extended tail towards larger radial actions. This evolution, albeit not very sizeable, is not

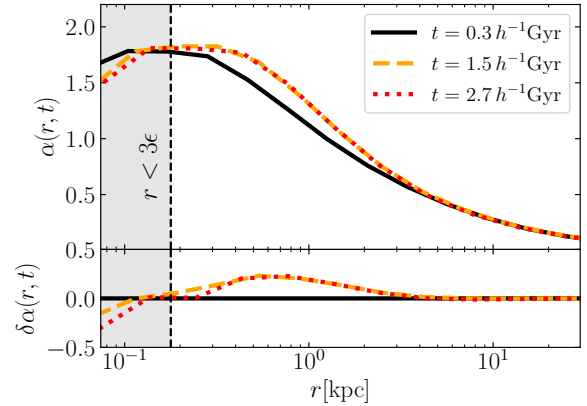


Figure 16. Logarithmic slope $\alpha(r, t)$ of the potential of the SIDM halo in Fig 13 as a function of radius at different times (upper panel) and change of the logarithmic slope with respect to $t = 0.3 h^{-1}\text{Gyr}$, also as a function of radius (lower panel). The times shown match the ones in Fig. 15. The grey shaded area highlights the resolution limit as in Fig. 13.

predicted by our formalism. In fact, our diffusion formalism predicts hardly any evolution at all, which might imply that this is a significant deviation. In Appendix C however, we show that the amplitude of the oscillation of radial actions in a potential developing a core is in general well approximated by our diffusion formalism. We thus surmise that the small but gradually increasing mismatch between the measured radial action and the result of the diffusion formalism is caused by numerical effects arising due to the discrete sampling of the SIDM halo. In fact, since the DM simulation particles are more massive than the tracers, individual close encounters between tracers and DM simulation particles can occasionally lead to a small sudden increase in the tracer’s energy, leading to a small increase in radial action as well.

Taking the prediction of our diffusion formalism at face value, we find that the evolution of $N(J_r, t)$ is fully adiabatic in a core-forming SIDM halo. Nevertheless, as we find in Appendix C, a shape-changing host potential can cause sizeable oscillations of the radial action values if the change in shape of the potential occurs fast enough. The fact that our diffusion theory does not predict any sizeable evolution of $N(J_r, t)$ thus implies that the change of the shape of $\Psi(r, t)$ is rather slow between $t = 0.3 h^{-1}\text{Gyr}$ and $t = 2.7 h^{-1}\text{Gyr}$. In Fig. 16, we look at the time evolution of the potential’s logarithmic slope $\alpha(r, t)$ of the evolving SIDM halo as a function of radius. We show the logarithmic slope of the potential at three different times, $t = 0.3 h^{-1}\text{Gyr}$ (solid black line), $t = 1.5 h^{-1}\text{Gyr}$ (dashed orange line) and $t = 2.7 h^{-1}\text{Gyr}$ (dotted red line). In the lower panel, we furthermore show the evolution of the logarithmic slope with respect to $t_0 = 0.3 h^{-1}\text{Gyr}$, defined as

$$\delta\alpha(r, t) = \alpha(r, t) - \alpha(r, t_0). \quad (68)$$

We find that the evolution of $\alpha(r, t)$, which directly impacts the ratio \dot{R}/R through the time-derivative $\dot{\alpha}(r, t)$, is most significant at earlier times and at smaller radii. In fact, in Fig. 16 we show that most of the evolution in $\alpha(r, t)$ occurs between $0.3 h^{-1}\text{Gyr}$ and $1.5 h^{-1}\text{Gyr}$. Afterwards, the shape of the potential is essentially constant. Given that Fig. 15

hardly shows any evolution of both predicted and measured $N(J_r, t)$ between $t = 0.3 h^{-1} \text{Gyr}$ and $t = 1.5 h^{-1} \text{Gyr}$, there should not be any physical evolution afterwards either, given that both the shape and the magnitude of $\Psi(r, t)$ are then approximately constant. We take this as confirmation that the small observed drift in this time interval is due to discreteness effects, i.e., it occurs because the potential is not perfectly smooth.

In conclusion, we find that SIDM with a cross section of $\sigma/m_\chi = 1 \text{ cm}^2 \text{g}^{-1}$ causes virtually no evolution in $N(J_r, t)$ and can thus be considered a fully adiabatic process. The drift and diffusion coefficients calculated within our diffusion formalism confirm this picture. When considering a cosmological SIDM halo, we note here that as the potential altering effects of mass accretion and SIDM peak at different times in cosmological simulations, since self-interactions only occur with a non-negligible probability above a certain density threshold (Vogelsberger et al. 2012), it is reasonable to look at those two effects as separate from each other. We stress, however, that in a cosmological SIDM halo the impact of mass accretion on the radial action distribution of tracers will far outweigh the impact of SIDM.

6 CONCLUSION

A statistical mechanics description of the out-of-equilibrium dynamics of a system of particles subject to long range forces has historically proven difficult for a variety of reasons. Negative specific heat and non-ergodicity of gravitating systems forbid the use of canonical or grand canonical ensembles. On top of that, Padmanabhan (1990) shows that in gravitating systems the energy is not an extensive parameter, thus the system cannot be divided into non-interacting macrocells and the laws of standard thermodynamics do not apply. On the other hand, N -body simulations of ever higher precision have yielded remarkably consistent results when simulating the collapse of cold dark matter (CDM) overdensities into virialized structures, so-called haloes. In fact, recently Wang et al. (2020) have shown that within the CDM model, the simulated inner structure of DM haloes is well described by a universal (cuspy) density profile over 20 orders of magnitude in halo mass, confirming the universality proposed in seminal papers two decades ago (Navarro et al. 1996b, 1997). Pontzen & Governato (2013) attempted to derive this universal profile using a maximum entropy approach. Following arguments from Jaynes (1957) information theory, they argue that the use of statistical mechanics to model the evolution of gravitating particle systems can still be applicable if additional physical constraints other than conservation of energy are taken into account. The authors then maximize the entropy under the condition that radial actions are conserved quantities. Traditionally, radial actions are assumed to be adiabatic invariants (see e.g. Binney & Tremaine (1987)), which means that they are exactly conserved if the change in time of the potential of the host happens sufficiently slowly. However, the maximum entropy approach by Pontzen & Governato (2013) fails to predict the cusp in the centre of CDM haloes due to a lack of particles with very low angular momentum.

Based on Lynden-Bell (1982), Peñarrubia (2013) developed a coordinate transformation relating the equations of motion in a frame with a time-dependent potential to the dynamics

in a different frame in which the potential is static. The integrals of motion in this new reference frame expressed in the coordinates of the original frame define so-called dynamical invariants. With the help of those, Peñarrubia (2015) develops a statistical theory to describe the diffusion of a gravitating particle ensemble in energy space. When discussing dynamical invariants, Peñarrubia (2013) further finds that radial actions of particles in time-dependent host potentials are not constant, but oscillate around a constant value with an amplitude which is proportional to the relative change of the gravitational potential $\dot{\Phi}/\Phi$.

The shortcomings of the work by Pontzen & Governato (2013), along with the finding of Peñarrubia (2013) that actions are not exact adiabatic invariants are the two main motivations for this work. In this paper, we set out to investigate whether and to what degree radial actions can be considered adiabatic invariants in time-dependent potentials of astronomical interest. To this end, we perform an analysis consisting of several steps. We first develop a general and exact expression for the linear (i.e. first order) variation of radial actions in time-dependent host potentials. Based on this, we develop and test a statistical theory for the diffusion of particle ensembles in radial action space. To illustrate a couple of relevant applications to this theory, we consider i) an idealised Milky-Way (MW) size halo with an evolving potential due to a mean cosmological mass accretion history, and ii) an evolving inner halo potential due to the cusp-core transformation of a dwarf-size self-interacting DM (SIDM) halo. A summary of our main methods and key results is as follows:

(i) *Calculating the linear variation of J_r .*— The starting point is to find a numerical (or approximate) solution to the differential equation for the scale-factor $R(t)$ which defines the coordinate transformation introduced in Peñarrubia (2013). We then show that we can write the radial action J'_r defined in the new time-independent reference frame in terms of the phase space coordinates of the particle in the original frame, where the potential is time-dependent. Under the assumption that the evolution of the latter is slow, we make a first order Taylor expansion of J'_r in the variable \dot{R}/R (see Section 2.2). We find that to zeroth order, the dynamical invariant J'_r and the radial action J_r in the original reference frame are the same. In line with our expectations, we find that the first order correction to this equality is indeed an oscillation with an amplitude proportional to \dot{R}/R and thus to $\dot{\Phi}/\Phi$ around the dynamical invariant. This oscillation happens in phase with the radial motion and is proportional to the radial period of the particle's orbit (see Eq. 19). We remark that this is the first time a model for the time-evolution of radial actions in time-dependent potentials has been developed. As a numerical test to this linear model, we follow the orbits of three tracer particles in a time-dependent analytic Keplerian potential using the N-body code AREPO (Springel 2010) (see Section 2.3). In case the first order term in the Taylor expansion is small compared to J_r itself, our linear model provides an excellent fit to the time-evolution of J_r (see left panel of Fig. 2). For orbits in the fringe of the potential ($E \approx 0$), such as the one shown in the right panel of Fig. 2, we find that the first order correction is of the order of J_r itself and thus the radial action evolves non-linearly and cannot be described by the first order Taylor expansion.

(ii) *Formulating a diffusion formalism in radial action space.* - Having calculated the linear variation of J_r for individual particles in a time-dependent potential, we then aim to statistically predict the evolution of the radial action distribution $N(J_r, t)$ of a particle ensemble. In Section 3.1, we show that if the time evolution of the gravitational potential is sufficiently slow, $N(J_r, t)$ is related to the invariant distribution of dynamical action invariants $N(J'_r)$ through a diffusion equation. The drift and diffusion coefficients $\tilde{C}(J_r, t)$ and $\tilde{D}(J_r, t)$ which appear in the diffusion equation are proportional to the ensemble average and the variance of the first order Taylor correction, respectively. We show that, by computing $\tilde{C}(J'_r, t)$ and $\tilde{D}(J'_r, t)$, we can calculate $N(J_r, t)$ from the invariant distribution $N(J'_r)$ through a simple Gaussian convolution. Based on what we found following individual tracer particles in Section 2.3, we define a criterion to determine whether or not the evolution of radial action distributions of a particle ensemble is expected to be accurately described by the diffusion formalism. Since the drift coefficient is zero in phase-mixed particle ensembles, we define three different regions in phase space dependent on the value of \tilde{D} relative to J_r :

- In the **linear** regime, $\sqrt{\tilde{D}} < 0.1 J_r$. We expect that the diffusion formalism will provide a good prediction of the evolution of $N(J_r, t)$ for particle distributions inhabiting this area in phase space.
- In the **transition** regime, $0.1 < \sqrt{\tilde{D}}/J_r < 1$ we expect (average) deviations from linear evolution, and thus our expectation is that the diffusion formalism will yield only rough results when applied to particle distributions in this part of phase space.
- In the **fringe**, $\sqrt{\tilde{D}} > J_r$, and thus we expect that the diffusion formalism does not apply.

To confirm these predictions, we perform a set of 5 restricted simulations of 20000 tracer particles orbiting in the same time-dependent Keplerian potential as the three individual tracers before and covering the phase space regions described above (see Table 1 and Fig. 3 for the simulation parameters and the restrictions in phase space). We find that a theoretical calculation of the diffusion coefficients in energy-action space agrees well with the coefficients measured from the initial tracer distributions (see Figs. 3–6). In the “10-linear” case (distribution centred at small radial actions $J_r = 10 h^{-1} \text{kpc km s}^{-1}$, and with energies mostly within the linear expectation), we show that when the drift and diffusion coefficients are measured directly from the particle distribution, the predictions of the diffusion formalism are in perfect agreement with direct measurements of both the invariant distribution $N(J'_r)$ and $N(J_r, t)$ at the end of the simulation (see Figs. 7, 8). Moreover, we find that a theoretical calculation of the diffusion coefficient yields equally sound results provided the drift coefficient is negligible, i.e., for fully phase-mixed particle ensembles (see Section 4.1 for a discussion). In general, we find that the agreement between the measured distribution and the prediction of the diffusion formalism deteriorates as a larger fraction of particles inhabits the “transition” area in phase space as opposed to the “linear” area (Section 4.2, Fig. 9). In consequence, since all tracers occupy the “transition” area in phase space close to the fringe in the “200-transition” case (distribution centred at large radial ac-

tions $J_r = 200 h^{-1} \text{kpc km s}^{-1}$, and with energies close to the fringe), the evolution of $N(J_r, t)$ in this case is highly non-linear and cannot be modelled as a diffusion process (see Section 4.3). We attempt to explain the observed evolution using higher-order perturbation theory (see Fig. 11 and Appendix B). However, we have to concede that while we manage to obtain an improved understanding of the shortcomings of the first order approximation, a full understanding of the non-linear evolution of $N(J_r, t)$ in the “fringe” remains beyond our reach. Phenomenologically, however, we observe that on average, there is a clear trend for particles whose evolution is non-linear to drift towards considerably smaller radial actions on the time-scales we simulate (see Figs. 1, 2, 10). In fact, particles whose actions are initially so large that there is no “linear” phase space available (see Fig. 3) tend to quickly drift towards values of J_r where this is no longer the case. We conclude that fast changes in the gravitational potential occurring over a short period of time can permanently alter the radial action distribution of particle ensembles affected by these changes. This effect is particularly important if the fraction of particles in the fringe area is significant while the change in gravitational potential occurs.

(iii) *Implications for halo mass accretion and cusp-core transformation.* - Since we can use the ratio between \tilde{D} and the radial action J_r to conclude whether the radial action distribution of a particle ensemble will evolve linearly or non-linearly, we can estimate whether radial actions are conserved quantities in gravitational systems of astrophysical interest. Using an approximate formula for the scale-factor of particles orbiting in a broken power law potential, we analyze whether radial action distributions evolve linearly throughout the accretion history of a MW-size halo and during the process of cusp-core transformation in a dwarf-size SIDM halo.

Mass accretion in a MW-size halo

To determine whether the mass accretion history of a typical MW-size halo allows for a linear evolution of radial actions, we determine the relative accretion rate \dot{M}/M as a function of redshift from the mass-redshift relation reported in [Boylan-Kolchin et al. \(2010\)](#). Subsequently, we determine the redshift at which the accretion rate is maximal and self-consistently sample the phase space coordinates of one million particles from the distribution function of a Hernquist halo with mass $M(z)$ and a scale radius $r_s(z)$ - both today and at the redshift of maximum accretion (see Section 5.1). Calculating $\tilde{D}(J_r, t)$ for each particle, we determine the fraction of particles inhabiting the “linear” part, the “transition” part and the “fringe” of the available energy-radial action phase space (see Fig. 12). We find that at the current time, the radial action distribution of particles in a MW-size halo evolves rather linearly, with 83 per cent of particles being in the “linear” regime of phase space. However, at the time of maximum accretion, we find that radial actions could not be considered conserved quantities on average. In fact, with 18 per cent of particles inhabiting the “fringe” and another 41 per cent being in the “transition” area in phase space, we expect a highly non-linear evolution on average. Furthermore, we find that at the redshift of maximum accretion, there is no linear phase space available for the largest radial actions. Following our discussion of non-linear evolution in the case of a time-dependent Keplerian potential, we deduce that the time-span

during which mass accretion into a MW-size halo is maximal can significantly alter the radial action distribution of particles within the halo by flattening the tail of the distribution and increasing the amount of particles with small radial actions. This suggests that radial action conservation cannot be taken as an additional physical constraint when attempting to derive the shape of DM haloes using statistical mechanics, as done by Pontzen & Governato (2013). It furthermore implies that an accurate modelling of the diffusion in radial action space can potentially improve the analysis of tidal streams in the MW.

We caution the reader that there are a few caveats to this result. Firstly, we have used an approximate expression for the scale-factor in a potential which is not scale-free. While we show in Appendix C that for generic spherical potentials this approximation is very good in case the evolution of J_r is “linear”, it is unclear how fast the approximation deteriorates for particles in the “transition” regime. However, we argue that this is unlikely to have a large impact on the conclusion that a significant amount of particles are not within the “linear” phase space area at the redshift at which accretion is maximal. Secondly, we use the approximation that for our purposes, the redshift-dependence of the halo concentration is simply given by $c_{200} \propto (1+z)^{-1}$. This is not a bad approximation, but it is not entirely true. To follow the full evolution of the scale radius, we would have to follow the evolution of the halo’s potential in a full cosmological simulation. This takes us to the last, most significant caveat of our analysis, which is that we have conducted it using a median relation for the accretion history of MW-size haloes. In reality, a large part of mass accretion happens through mergers, which produce a more impulsive and step-wise change of the halo’s mass than the continuous/smooth median mass accretion assumed here. The model presented here can thus serve as an educated guess about how mass accretion affects the radial action distribution of the DM particles, but an accurate description of how exactly $N(J_r, t)$ evolves requires a more in-depth modelling of the halo’s merger history.

Cusp-core transformation in a dwarf-size SIDM halo

Finally, we investigate whether cusp-core transformation in a dwarf-size halo of self-interacting dark matter (SIDM) leads to a linear or non-linear evolution of radial action distributions of tracer particles (see Section 5.2). We re-run the SIDM simulation of table 1 in Burger & Zavala (2019), increasing the number of tracer particles by a factor of ten and changing the self-scattering cross section to $\sigma/m_\chi = 1 \text{ cm}^2 \text{ g}^{-1}$, a value which is around the current constraint on SIDM at dwarf scales (Read et al. 2018). We take snapshots every $100 h^{-1} \text{ Myr}$ and closely follow the orbits of the tracers at each time step. We use the same approximate functional form for the scale factor as we did when analyzing the accretion history of a MW-size halo. However, we now take the changing halo shape into account when calculating its time derivative. At each snapshot, we calculate the fraction of DM particles in the “linear” and the “transition” regime as well as the “fringe” by calculating \tilde{D} and J_r for each particle. We find that the fraction of particles in the linear regime is never below 97 per cent (see Fig. 14 and conclude that cusp-core transformation due to SIDM leads to a very slow change in the halo’s potential, implying that the evolution of radial action distributions

of particles orbiting in the SIDM halo is adiabatic and can be described using our diffusion formalism.

When following the orbits of all tracers throughout the simulation, we find that the radial action distribution is nearly constant, confirming our conjecture that it will evolve linearly. The diffusion formalism predicts that $N(J_r, t)$ hardly changes at all during core formation. However, the measured radial action distribution gradually develops a tail towards larger radial actions that extends beyond the prediction made by the diffusion formalism (see Fig. 15). For that reason, we test in Appendix C whether the use of the approximate scale factor $R(t)$ is valid in potentials with a time-dependent shape. We find that when modelling core formation in a smooth external potential rather than a live halo, and using the approximate scale factor, the linear Taylor expansion of the time evolution of J_r is in very good agreement with the directly measured evolution. Furthermore, we show that during the time in which the extended tail forms in the measured $N(J_r, t)$, the shape of the potential is largely constant (see Fig. 16), implying that radial actions should be conserved during that time. Because of that, we conclude that the observed evolution of $N(J_r, t)$ is caused by individual close encounters between kinematic tracers and DM (simulation) particles and is thus a numerical effect. In consequence, we take the prediction of our diffusion formalism at face value and deduce that core formation in dwarf-sized haloes due to SIDM with a self-interaction cross-section of $\sigma/m_\chi = 1 \text{ cm}^2 \text{ g}^{-1}$ has no detectable impact on the radial actions of kinematic tracers. In other words, it is fully adiabatic.

In summary, we have, for the first time, developed a model for the time evolution of radial actions in time-dependent spherical potentials. Based on that, we have developed a diffusion theory for radial action distributions of particle ensembles subject to time-dependent gravitational potentials. This diffusion theory relates the evolution of the distribution $N(J_r, t)$ to an invariant distribution $N(J'_r)$ in a frame which is related to the time-dependent frame via a coordinate transformation defined by a scale-factor. We have demonstrated the validity of our formalism, and furthermore provided a discussion of its limitations, by performing restricted N -body simulations of tracer particles with different initial distributions in radial action and applying the diffusion formalism to model how these distributions evolve with time. We have shown that the size of the diffusion coefficient $\tilde{D}(J_r, t)$ relative to the square of the radial action itself is a good indicator for whether radial action distributions will evolve linearly or not, and thus for whether the diffusion formalism we developed is applicable. We have furthermore shown that highly non-linear evolution most often entails a drift of radial action distributions to lower actions. We have then applied our mechanism to two distinct cases of interest in astrophysics. Firstly, we have argued that on average, radial actions are likely not to be conserved over the mass accretion history of a MW-size halo, and that the accretion history of a halo is likely to leave an imprint in the radial action distribution of a halo. Secondly, we have shown that radial action distributions evolve linearly in a core-forming dwarf-size SIDM halo, implying that SIDM gives rise to an adiabatic change of a halo’s gravitational potential.

While we have shown that the approximate scale factor yields valid results when applied to potentials with a chang-

ing shape, we note that it is derived assuming that its time-derivative is constant. This implies that its applicability is at least questionable when moving towards the “transition” regime in phase space. One of the biggest challenges for future work lies in finding more general solutions for the scale-factors in different classes of spherical potentials. Extending our formalism to actions that are defined in non-spherical coordinate systems should be straight-forward. For future work, our goal is to use the formalism developed here to further investigate the interdependence between the universal CDM halo density profile and the accretion history of CDM haloes.

ACKNOWLEDGEMENTS

We thank Volker Springel for giving us access to the AREPO code. JB and JZ acknowledge support by a Grant of Excellence from the Icelandic Center for Research (Rannís; grant number 173929). The simulations in this paper were carried out on the Garpur supercomputer, a joint project between the University of Iceland and University of Reykjavík with funding from Rannís.

REFERENCES

- Antonov V. A., 1961, *Soviet Ast.*, **4**, 859
 Arad I., Johansson P. H., 2005, *MNRAS*, **362**, 252
 Binney J., Tremaine S., 1987, *Galactic dynamics*
 Boylan-Kolchin M., Springel V., White S. D. M., Jenkins A., 2010, *Monthly Notices of the Royal Astronomical Society*, **406**, 896
 Buist H. J. T., Helmi A., 2015, *A&A*, **584**, A120
 Bullock J. S., Boylan-Kolchin M., 2017, *ARA&A*, **55**, 343
 Burger J. D., Zavala J., 2019, *MNRAS*, **485**, 1008
 Colín P., Avila-Reese V., Valenzuela O., Firmani C., 2002, *ApJ*, **581**, 777
 Davé R., Spergel D. N., Steinhardt P. J., Wandelt B. D., 2001, *ApJ*, **547**, 574
 Dehnen W., 1993, *MNRAS*, **265**, 250
 Eddington A. S., 1916, *MNRAS*, **76**, 572
 Einstein A., 1905, *Annalen der Physik*, **322**, 549
 Goodman J., Binney J., 1984, *MNRAS*, **207**, 511
 Jaynes E. T., 1957, *Physical Review*, **106**, 620
 Kaplinghat M., Tulin S., Yu H.-B., 2016, *Phys. Rev. Lett.*, **116**, 041302
 Kuzio de Naray R., McGaugh S. S., de Blok W. J. G., 2008, *ApJ*, **676**, 920
 Levin Y., Pakter R., Rizzato F. B., 2008, *Phys. Rev. E*, **78**, 021130
 Levin Y., Pakter R., Rizzato F. B., Teles T. N., Benetti F. P. C., 2014, *Phys. Rep.*, **535**, 1
 Ludlow A. D., Navarro J. F., Angulo R. E., Boylan-Kolchin M., Springel V., Frenk C., White S. D. M., 2014, *MNRAS*, **441**, 378
 Lynden-Bell D., 1967, *MNRAS*, **136**, 101
 Lynden-Bell D., 1982, *The Observatory*, **102**, 86
 Lynden-Bell D., 1999, *Physica A Statistical Mechanics and its Applications*, **263**, 293
 Lynden-Bell D., Lynden-Bell R. M., 1977, *MNRAS*, **181**, 405
 Moore B., 1994, *Nature*, **370**, 629
 Nakamura T. K., 2000, *ApJ*, **531**, 739
 Navarro J. F., Eke V. R., Frenk C. S., 1996a, *MNRAS*, **283**, L72
 Navarro J. F., Frenk C. S., White S. D. M., 1996b, *ApJ*, **462**, 563
 Navarro J. F., Frenk C. S., White S. D. M., 1997, *ApJ*, **490**, 493
 Navarro J. F., et al., 2010, *MNRAS*, **402**, 21
 Padmanabhan T., 1989, *ApJ*, **344**, 848
 Padmanabhan T., 1990, *Phys. Rep.*, **188**, 285
 Peñarrubia J., 2013, *MNRAS*, **433**, 2576

- Peñarrubia J., 2015, *MNRAS*, **451**, 3537
 Peñarrubia J., 2019, *MNRAS*, **484**, 5409
 Pontzen A., Governato F., 2012, *Mon. Not. Roy. Astron. Soc.*, **421**, 3464
 Pontzen A., Governato F., 2013, *MNRAS*, **430**, 121
 Power C., Navarro J. F., Jenkins A., Frenk C. S., White S. D. M., Springel V., Stadel J., Quinn T. R., 2003, *Mon. Not. Roy. Astron. Soc.*, **338**, 14
 Read J. I., Walker M. G., Steger P., 2018, *MNRAS*, **481**, 860
 Robles V. H., et al., 2017, *MNRAS*, **472**, 2945
 Rocha M., Peter A. H. G., Bullock J. S., Kaplinghat M., Garrison-Kimmel S., Oñorbe J., Moustakas L. A., 2013, *MNRAS*, **430**, 81
 Sánchez-Conde M. A., Prada F., 2014, *MNRAS*, **442**, 2271
 Sanderson R. E., Helmi A., Hogg D. W., 2015, *ApJ*, **801**, 98
 Sanderson R. E., Hartke J., Helmi A., 2017, *ApJ*, **836**, 234
 Santos-Santos I. M. E., et al., 2020, *MNRAS*, **495**, 58
 Spergel D. N., Steinhardt P. J., 2000, *Physical Review Letters*, **84**, 3760
 Springel V., 2010, *Mon. Not. Roy. Astron. Soc.*, **401**, 791
 Springel V., et al., 2005, *Nature*, **435**, 629
 Turner H. C., Lovell M. R., Zavala J., Vogelsberger M., 2020, arXiv e-prints, [p. arXiv:2010.02924](https://arxiv.org/abs/2010.02924)
 Vogelsberger M., Zavala J., Loeb A., 2012, *MNRAS*, **423**, 3740
 Vogelsberger M., Zavala J., Simpson C., Jenkins A., 2014, *MNRAS*, **444**, 3684
 Walker M. G., Peñarrubia J., 2011, *ApJ*, **742**, 20
 Wang J., Bose S., Frenk C. S., Gao L., Jenkins A., Springel V., White S. D. M., 2020, *Nature*, **585**, 39
 Yoshida N., Springel V., White S. D. M., Tormen G., 2000, *ApJ*, **544**, L87
 Zavala J., Frenk C. S., 2019, *Galaxies*, **7**, 81
 Zavala J., Vogelsberger M., Walker M. G., 2013, *MNRAS*, **431**, L20
 Zavala J., Lovell M. R., Vogelsberger M., Burger J. D., 2019, *Phys. Rev. D*, **100**, 063007
 de Blok W. J. G., Walter F., Brinks E., Trachternach C., Oh S.-H., Kennicutt Jr. R. C., 2008, *AJ*, **136**, 2648

APPENDIX A: NUMERICAL CALCULATION OF THE SCALE-FACTOR

In this section we discuss how we calculate the scale-factor $R(t)$ numerically using Eq. (8). We start by recalling that Eq. (8) has an analytic solution if the evolution is adiabatic. In this case we can neglect the term proportional to the second derivative of the scale-factor. We can then write

$$R^3 \mathbf{F}(R\mathbf{r}', t) = \mathbf{F}'(\mathbf{r}'). \quad (\text{A1})$$

Using Eqs. (2) and (4), we can write

$$-R^3 \frac{GM_0(1+\epsilon t)}{(Rr')^2} = -\frac{GM_0}{(r')^2} \quad (\text{A2})$$

$$R(t) = \frac{1}{(1+\epsilon t)} \quad (\text{A3})$$

which leads to

$$\frac{\dot{R}}{R} = -\frac{\epsilon}{\epsilon + t}. \quad (\text{A4})$$

Up to first order, the scale-factor only depends on time, and there is no residual dependence on the orbital trajectory of individual tracer particles. In this paper, however, we are particularly interested in both the fully adiabatic regime and the regime in which the evolution of tracer particles' radial actions is non-adiabatic. For individual tracers, adapting

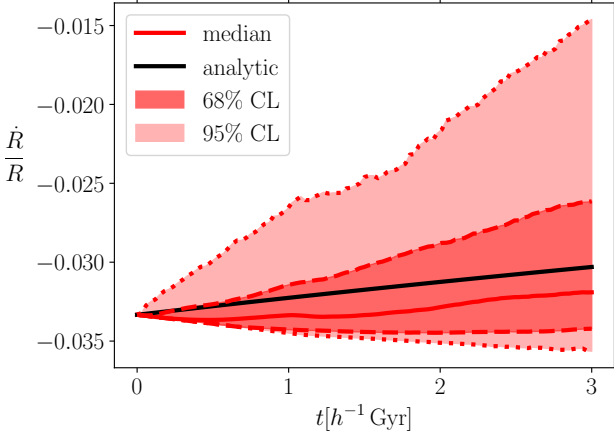


Figure A1. Confidence level regions of \dot{R}/R versus time, taken from the “10-linear” simulation. The solid red line shows the median value, the dark red shaded region shows the 68% CL and the light red shaded region shows the 95% CL. The analytic solution from Eq. (A4) is shown as a solid black line.

Eq. (A3) as the scale-factor might thus be a bad approximation in particular when $\sqrt{R/\dot{R}}$ is on the order of the radial period.

To avoid this issue, we solve Eq. (8) numerically along the phase space trajectory of each particle, using a KDK leapfrog algorithm. First, we rewrite Eq. (8) for the Keplerian case as

$$\ddot{R}R^3r' + R^3\frac{GM(t)}{R^2r'^2} = \frac{GM(0)}{r'^2}, \quad (\text{A5})$$

and using $r = Rr'$ we can write this as

$$\ddot{R}R^2r + R^3\frac{GM(t)}{r^2} = \frac{GM(0)}{r^2} \quad (\text{A6})$$

$$\ddot{R} = -R\frac{GM(t)}{r^3} + \frac{GM(0)}{r^3} = G(R(t), r(t), t). \quad (\text{A7})$$

During the simulation, we record phase space coordinates at each time step, as well as the simulation time. Calling the size of one time step in the simulation Δt , we then evolve Eq. A7 between times t and $t + \Delta t$ as follows:

$$\dot{R}\left(t + \frac{\Delta t}{2}\right) = \dot{R}(t) + \frac{\Delta t}{2}G(R(t), r(t), t) \quad (\text{A8})$$

$$R(t + \Delta t) = R(t) + \Delta t\dot{R}\left(t + \frac{\Delta t}{2}\right) \quad (\text{A9})$$

$$\begin{aligned} \dot{R}(t + \Delta t) &= \dot{R}\left(t + \frac{\Delta t}{2}\right) \\ &+ \frac{\Delta t}{2}G(R(t + \Delta t), r(t + \Delta t), t + \Delta t). \end{aligned} \quad (\text{A10})$$

Since Eqs. (A8), (A9) and (A10) explicitly depend on the radius at a given time, there is now an orbit-dependent part that enters. We thus assume that the first order estimate Eq. (A4) is not correct for all particles. Instead, we expect that the true values of \dot{R} will be distributed around the analytic solution given by Eq. (A3).

Fig. A1 shows the median of \dot{R}/R versus time as a red solid line, calculated from the “10-linear” case defined in table 1.

The 68% (and 95%) confidence level regions are shown as dark (and light) red shaded areas. The analytic approximate solution of Eq. (A4) is shown as a black solid line. Both the median and the analytic solution lie well within the 68% confidence level. Overall, we find that the analytic solution is a reasonable approximation for most particles.

A small fraction of particles tends towards significantly (50 per cent) larger values of \dot{R}/R as time progresses, yet the median stays close to the analytic solution at all times. This suggests that in the “10-linear” case, which is closest to being adiabatic, the analytic solution to Eq. (A5) provides a good approximation of the true scale-factor.

APPENDIX B: HIGHER ORDER PERTURBATION THEORY

The formalism presented in Sections 3 and 4 focuses on linear perturbation theory and a diffusion formalism developed by deriving drift- and diffusion coefficients from the linear variation of the radial action in a time-dependent potential. Here we discuss a possible variations of this formalism. We calculate the radial action evolution to higher orders in perturbation theory, allowing for a slightly more accurate description of radial actions inhabiting the “transition” area between the “linear” regime and the “fringe”.

Eq. (17) is a general expansion of the invariant radial action J'_r , which equates the difference between J'_r and J_r to an infinite Taylor series. In Eq. 19, however, we truncate this series after the first order assuming that the perturbations to the radial action are small on average. But as we have seen throughout Section 4, the linear correction is not valid in the “fringe” of the potential. Within the “transition” area, we find that the diffusion algorithm based on the Taylor expansion up to linear order gradually deteriorates. Hereafter, we calculate the second order corrections and investigate how including them affects the results of the diffusion formalism.

To calculate J_r to the second order in perturbation theory, we need to use the exact (higher order) version of Eq. (9), which is (see Peñarrubia (2013))

$$\frac{I}{R^2} = E - \frac{\dot{R}}{R}(\mathbf{r} \cdot \mathbf{v}) + \frac{1}{2}\left(\frac{\ddot{R}}{R} + \left(\frac{\dot{R}}{R}\right)^2\right). \quad (\text{B1})$$

Hereafter, we formally develop the second order of perturbation theory. First, let us look at the invariant action in the time-independent reference frame

$$J'_r = \int_{r'_{\text{peri}}}^{r'_{\text{apo}}} dr' \sqrt{2I - 2\tilde{\Phi}(\mathbf{r}') - \frac{L^2}{r'^2}} \quad (\text{B2})$$

Since I is a true dynamical invariant, changing between coordinate systems and writing I in terms of time-dependent quantities cannot result in I depending on phase space variables. The integral Eq. (B2) is thus always defined solely in the static frame, but we are allowed to write the constants and functions appearing in the integral as functions of time-dependent quantities, as long as the integrand depends on the integration variable in the same way.

The defining equation relating the potentials in both frames is

$$\tilde{\Phi}(\mathbf{r}') = \frac{1}{2}R\ddot{R}r'^2 + R^2\Phi(\mathbf{r}, t) \quad (\text{B3})$$

which we can rewrite in terms of r' as

$$\tilde{\Phi}(\mathbf{r}') = \frac{1}{2}R^3\ddot{R}r'^2 + R^2\Phi(R\mathbf{r}', t) \quad (\text{B4})$$

If the potential is scale-free, this enables us to write the integrand of Eq. (B2) in terms of time-dependent quantities while still keeping all dependence on the integration variable explicit and analytic. Note that to do so we have to use $\dot{R} = 0$ in Eq. (B4) for consistency, since we originally used this assumption in Eq. (8) to obtain scale-factors which do not depend on the phase-space trajectory of each particle.

In potentials with a scale, the scale-factor can in general not be treated as independent of the phase space trajectory. This implies that writing the potential in the time-independent frame in terms of time-dependent quantities introduces an implicit and thus non-analytic dependence on the integration variable (the radius) through the scale factor. This does not alter the linear correction, provided we take the following (adiabatic) limit.

The key assumption is that even if the potential is not scale-free, we can approximate the scale-factor as independent of the particle's trajectory on time-scales which are of the order of one orbital time. This means that the scale-factor, and hence the potential, evolves slowly compared to the particle's orbital period, which is exactly what defines the adiabatic regime. Mathematically, this means that since we evaluate Eq. (B1) at a fixed time and we treat R in Eq. (B4) as dependent on time only, we can treat R as a simple scalar when evaluating the integral B2.

To expand Eq. (B2), we first introduce a few definitions. We define

$$f'(r') = 2I - 2\tilde{\Phi}(\mathbf{r}') - \frac{L^2}{r'^2} \quad (\text{B5})$$

as the square of the integrand in the static frame. Then we define the functions $g'(I, L)$ and $h'(I, L)$ as the peri- and apocentre radii of particles with energy I and angular momentum L . Next, we define

$$f(\mathbf{r}', y, z) = 2E - 2y(\mathbf{r} \cdot \mathbf{v}) + r^2(z + y^2) - R^2 z r'^2 - 2\Phi(R\mathbf{r}', t) - \frac{L^2}{R^2 r'^2}, \quad (\text{B6})$$

which is $f = R^2 f'$ with the energy and the potential written in terms of time-dependent quantities. Here we have further introduced $y = \dot{R}/R$ and $z = \ddot{R}/R$ as the variables in which we Taylor expand later on. Finally, we define $g(E, L, y, z)$ and $h(E, L, y, z)$ as $g = Rg'$, $h = Rh'$. It is straight-forward to show that they reduce to the peri- and apocenter radii in the time-dependent frame when taking the limit $y \rightarrow 0$, $z \rightarrow 0$. Under the assumption that R is independent of the orbital trajectory, we can write $R dr' = dx$ and

$$J'_r = \int_{g(E, L, y, z)}^{h(E, L, y, z)} dx k(\mathbf{x}, y, z), \quad (\text{B7})$$

where $k(\mathbf{x}, y, z) = \sqrt{f(\mathbf{x}, y, z)}$ and

$$f(\mathbf{x}, y, z) = 2E - 2y(\mathbf{r} \cdot \mathbf{v}) + r^2(z + y^2) - z x^2 - 2\Phi(\mathbf{x}, t) - \frac{L^2}{x^2}, \quad (\text{B8})$$

It is thus evident that

$$J'_r|_{y, z \rightarrow 0} = J_r \quad (\text{B9})$$

For the first order in y , we have to calculate

$$\begin{aligned} \frac{\partial J'_r}{\partial y} &= \int_{g(E, L, y, z)}^{h(E, L, y, z)} dx \frac{\partial k(\mathbf{x}, y, z)}{\partial y} \\ &+ k(h(E, L, y, z), y, z) \frac{\partial h}{\partial y} - k(g(E, L, y, z), y, z) \frac{\partial g}{\partial y}. \end{aligned} \quad (\text{B10})$$

If we take the limit, it is easy to show that we recover:

$$\left. \frac{\partial J'_r}{\partial y} \right|_{y, z \rightarrow 0} = -(\mathbf{r} \cdot \mathbf{v}) \frac{P(E, L)}{2\pi} \quad (\text{B11})$$

To go to higher orders, we have to calculate

$$\begin{aligned} \frac{\partial J'_r}{\partial z} &= \int_{g(E, L, y, z)}^{h(E, L, y, z)} dx \frac{\partial k(\mathbf{x}, y, z)}{\partial z} \\ &+ k(h(E, L, y, z), y, z) \frac{\partial h}{\partial z} - k(g(E, L, y, z), y, z) \frac{\partial g}{\partial z} \end{aligned} \quad (\text{B12})$$

and

$$\begin{aligned} \frac{\partial^2 J'_r}{\partial y^2} &= \int_{g(E, L, y, z)}^{h(E, L, y, z)} dx \frac{\partial^2 k(\mathbf{x}, y, z)}{\partial y^2} \\ &+ 2 \frac{\partial k(h(E, L, y, z), y, z)}{\partial y} \frac{\partial h}{\partial y} \\ &- 2 \frac{\partial k(g(E, L, y, z), y, z)}{\partial y} \frac{\partial g}{\partial y} \\ &+ \frac{\partial k(h(E, L, y, z), y, z)}{\partial h(E, L, y, z)} \left(\frac{\partial h}{\partial y} \right)^2 \\ &- \frac{\partial k(g(E, L, y, z), y, z)}{\partial g(E, L, y, z)} \left(\frac{\partial g}{\partial y} \right)^2 \\ &+ k(h(E, L, y, z), y, z) \frac{\partial^2 h}{\partial y^2} \\ &- k(g(E, L, y, z), y, z) \frac{\partial^2 g}{\partial y^2}. \end{aligned} \quad (\text{B13})$$

We can then write

$$J'_r = J_r + A \frac{\dot{R}}{R} + B \frac{\ddot{R}}{R} + \frac{1}{2} C \left(\frac{\dot{R}}{R} \right)^2, \quad (\text{B14})$$

with

$$A = \left. \frac{\partial J'_r}{\partial y} \right|_{y, z \rightarrow 0}, \quad (\text{B15})$$

$$B = \left. \frac{\partial J'_r}{\partial z} \right|_{y, z \rightarrow 0} \quad (\text{B16})$$

and

$$C = \left. \frac{\partial^2 J'_r}{\partial y^2} \right|_{y, z \rightarrow 0}. \quad (\text{B17})$$

We note that if we stop the expansion here, we implicitly assume that \dot{R}/R is of the same order as $(\dot{R}/R)^2$. In the Keplerian example, we can verify this and find from Eq. (A3) that $\dot{R}/R = 2\ddot{R}/R$ in the adiabatic limit.

In general, the integrals defining the coefficients A, B, C in Eq. (B14) have to be evaluated numerically. The limits then also have to be taken numerically. This is usually quite complicated and a lot of effort, given that what we hope to achieve here is a slightly better understanding of the evolution of radial action distributions in the "transition" regime of Fig.

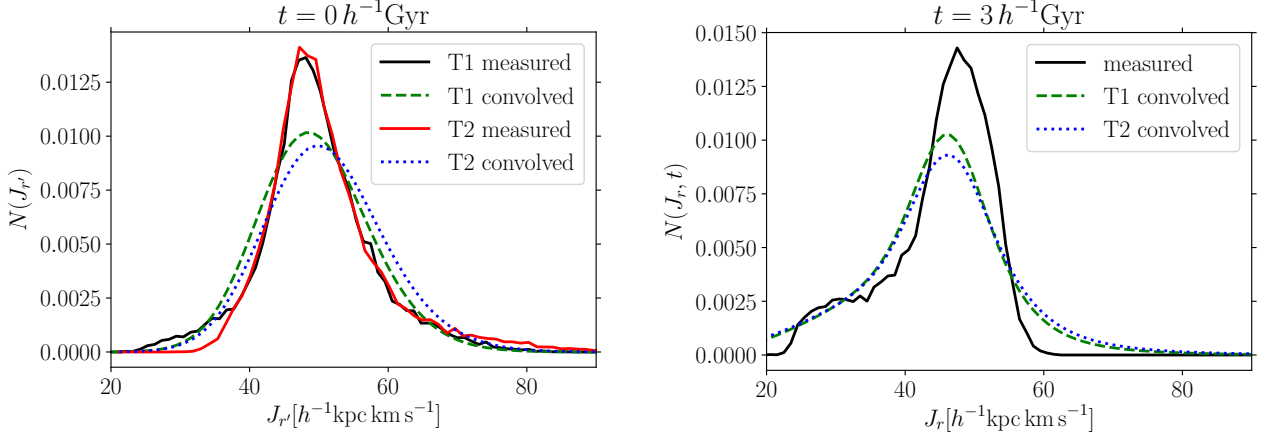


Figure B1. First order Taylor expansion (T1) and second order Taylor expansion (T2) in comparison in the “50-transition” case. The left panel shows the invariant distribution calculated at $t = 0$. The black and red line are directly measured distributions obtained by binning J'_r of each particle. The red line is calculated applying the second order Taylor expansion to calculate J'_r , whereas the black line is calculated using the first order expansion. The green dashed line is the result of a Gaussian convolution, with drift and diffusion coefficients calculated from the first order Taylor expansion. The blue dotted line is the result of a convolution using the second order Taylor expansion. On the right panel, we see the measured radial action distribution in the time-dependent frame in black, calculated at $t = 3 h^{-1} \text{Gyr}$. The result of the first order diffusion formalism is shown as a green dashed line and compared to the result of the second order diffusion formalism which is shown as a blue dotted line.

3. Fortunately, in the case of the Keplerian potential, we can calculate the invariant action explicitly as

$$J'_r = \frac{GM_0}{\sqrt{-2I}} - L \quad (\text{B18})$$

If we Taylor expand the invariant action up to the second order, we find

$$\begin{aligned} J_r = J'_r + \frac{GM}{\sqrt{2\mathcal{E}^3}} (\mathbf{r} \cdot \mathbf{v}) \frac{\dot{R}}{R} \\ - \frac{1}{2} \frac{GM}{\sqrt{2\mathcal{E}^3}} r^2 \left(\left(\frac{\dot{R}}{R} \right)^2 + \frac{\ddot{R}}{R} \right) \\ - \frac{3}{2} \frac{GM}{\sqrt{2\mathcal{E}^5}} (\mathbf{r} \cdot \mathbf{v})^2 \left(\frac{\dot{R}}{R} \right)^2. \end{aligned} \quad (\text{B19})$$

From Eq. (B19) we see that second order corrections become important at larger energies, meaning when we are moving closer to the “fringe”. Let us investigate the impact of including second order corrections on the 50-transition case of Section 4.

In Fig. B1 we compare the results of the diffusion formalism in the “50-transition” case when using first order coefficients (T1) and second order coefficients (T2). The left panel compares the invariant distributions obtained at the beginning of the simulation. The “measured” curves refer to a direct measurement of the distributions, where in order to measure the “T1” distribution we have applied the first order correction to the action of each individual particle and then calculated $N(J'_r)$ by binning the particles in J'_r . Accordingly, the “T2” distribution is the result of applying the second order correction instead of the first order correction to calculate each particle’s invariant action.

The “convolved” curves are the results of applying the Gaussian convolution defined in Eq. (46), using drift and diffusion coefficients obtained from the first order Taylor ex-

pansion (T1) and the second order Taylor expansion (T2) respectively. Overall, we find that “T1 measured” and “T2 measured” look very similar when compared to each other. The same is true for “T1 convolved” and “T2 convolved”, implying that including second order corrections does not change the overall picture much.

The effect of including the second order coefficients is mainly to erase the tail at the lower end of the distribution and introduce a tail at the higher end of the distribution instead. This is to some extent expected, as the second order corrections all increase the value of J'_r (see Eq. (B19)). Comparing the “T1” curves to the “T2” curves, we find no significant improvement of the match between the “measured” and the “convolved” curves. We note that, as the tails of the invariant distribution in particular seem to be very sensitive to the order of perturbation theory, we can expect higher orders to have a sizeable impact as well.

In the right panel of Fig. B1 we show the final result obtained from Eq. (47), using the distributions on the left panel and drift and diffusion coefficients calculated at $t = 3 h^{-1} \text{Gyr}$. Again, “T1” refers to the first order Taylor expansion result, whereas “T2” refers to the result when using drift and diffusion coefficients calculated from the second order Taylor expansion. Evidently, the agreement between the measured distribution and the result of the diffusion formalism does not improve significantly when using second order coefficients. The most obvious effect is that the second order result has a slightly more extended tail towards larger radial actions, which is, however, hardly significant. The tail on the lower action side is still resolved quite well in both cases. All in all, the diffusion formalism captures some key results of the evolution of the action distribution, but remains unable to resolve the “50-transition” distribution to high accuracy.

It is no surprise that the diffusion formalism becomes increasingly less applicable when moving towards the “fringe” of

the gravitational potential, i.e. the cyan and red areas in Fig. 3. We conclude that the evolution of the "50-transition" case is at least partly non-perturbative and cannot be fully captured by the diffusion formalism derived in Section 3. Nonetheless, the second order correction still represents a more accurate approximation of the invariant action of individual particles inhabiting the transition regime. We can thus use it to gain additional insight into the non-linear evolution of $N(J_r, t)$ in the "200-transition" simulation.

APPENDIX C: AN APPROXIMATE SCALE FACTOR FOR GENERIC SPHERICAL POTENTIALS

In the case of scale-free power law potentials, Peñarrubia (2013) has shown that in the adiabatic limit, an approximate solution to Eq. (8) is given by Eq. (37). In Appendix A, we compare this approximate scale factor to a distribution of numerically calculated scale factors of a set of tracer particles orbiting in a time-dependent Keplerian potential. We find an overall good agreement between the approximate scale factor and the median of the distribution of numerically calculated scale factors. For many applications of physical interest, it is desirable to obtain an approximate scale factor for generic spherical potentials which are not scale-free. Under certain assumptions, we can find an approximate solution to Eq. (8). If we assume that the force can be written as

$$\mathbf{F}(\mathbf{r}, t) = F(t) r^{\beta(r, t)} \frac{\mathbf{r}}{r}, \quad (\text{C1})$$

where $\beta(r)$ is now a local power law index, we can find an approximate solution to Eq. (8) in the adiabatic limit, which is

$$R_1(t) = \left(\frac{F(r, t)}{F(r, 0)} \right)^{-\frac{1}{(3+\beta(r, t))}}, \quad (\text{C2})$$

where $F(r, t)$ denotes the local time-dependent magnitude of the force. Peñarrubia (2013) shows that Eq. (8) can also be integrated, leading to an equation that relates the time-dependent potential to the constant potential in the time-invariant frame. An approximate solution to this integrated equation is

$$R_2(t) = \frac{1}{2 + \alpha(r, t)} \left(\frac{\Phi(r, t)}{\Phi(r, 0)} \right)^{-\frac{1}{2 + \alpha(r, t)}}, \quad (\text{C3})$$

where

$$\alpha(r, t) = \frac{d \log(-\Phi(r, t))}{d \log r}. \quad (\text{C4})$$

It is worth noting, however, that the potential $\Phi(r, t)$ is only defined up to an integration constant. In most N-body codes, this constant is used to fix the limit of the potential at large radii to $\Phi(r \rightarrow \infty, t) = 0$. For the potentials of most self-gravitating systems, such as a Plummer, Hernquist or NFW potential, this implies $\Phi(r \rightarrow 0, t) = \text{const}$, and thus a local power law index of $\alpha(0, t) = 0$, irrespective of the behaviour of the force. However, in order for Eq. (C3) to be consistent with Eq. (C2), we demand that $\alpha(0, t) = 1 + \beta(0, t)$, in order to match the case of scale-free potentials. We can recover this behaviour by setting the integration constant to zero when calculating the potential, or equivalently, by defining

$$\Psi(r, t) = \Phi(r, t) - \Phi(0, t). \quad (\text{C5})$$

Then, we can calculate the scale-factor as

$$R_3(t) = \frac{1}{2 + \alpha(r)} \left(\frac{\Psi(r, t)}{\Psi(r, 0)} \right)^{-\frac{1}{2 + \alpha(r)}}, \quad (\text{C6})$$

where

$$\alpha(r) = \frac{d \log(\Psi(r, t))}{d \log r}. \quad (\text{C7})$$

When calculating the first order correction term to the radial action in Eq. (19), the relevant quantity is not the scale factor itself, but its normalized time derivative \dot{R}/R . In the case of core formation due to SIDM, which we discuss in Section 5.2, both the time evolution of the gravitational potential and the time-evolution of the potential's logarithmic slope can be sizeable. This can cause two potential problems. Firstly, the approximate solutions (Eqs. (C2), (C3) and (C6)) are derived under the assumption of constant local power law slopes, and it is thus not clear whether they will hold in a potential with a time-dependent shape. Moreover, the time-dependence of the power law slopes differs between Eqs. (C2), (C3) and (C6), both due to the impact of the integration constant on the power law index of the potential, and because in generic spherical potentials, there is not a single one-to-one correspondence between the power law indices of the force and the potential (i.e. $\alpha = 1 + \beta$ is never true for all radii in potentials with a scale).

Here, we perform a short numerical test to determine whether we can use the approximate scale factors to describe the evolution of potentials with a time-dependent shape. We closely follow the orbits of kinematic tracers in the potential generated by a time-dependent Dehnen (1993) density profile:

$$\rho(r, t) \propto r^{-\gamma(t)} (r + r_s)^{\gamma(t)-4} \quad (\text{C8})$$

We fix the normalization of the density profile by enforcing mass conservation. At each point in time we normalize the density profile such that

$$M(< r_{200}) = 10^{10} h^{-1} M_{\odot}, \quad (\text{C9})$$

where $r_{200} = 35.1 h^{-1} \text{kpc}$. The scale radius r_s is then fixed by setting $c_{200} = 15$. We model the transition from a cuspy to a cored profile by fixing the power law slope as:

$$\gamma(t) = 1 - \frac{t}{t_{\text{max}}}, \quad (\text{C10})$$

where $t_{\text{max}} = 3 h^{-1} \text{Gyr}$ is the total simulation time. We then closely follow the orbits of kinematic tracers and numerically calculate the radial action at each timestep, similar to Fig. 2. Additionally, we also calculate the first order Taylor expansion of J_r defined in Eq. (19) using the scale factors R_1 , R_2 and R_3 defined above. To that end, we estimate their time

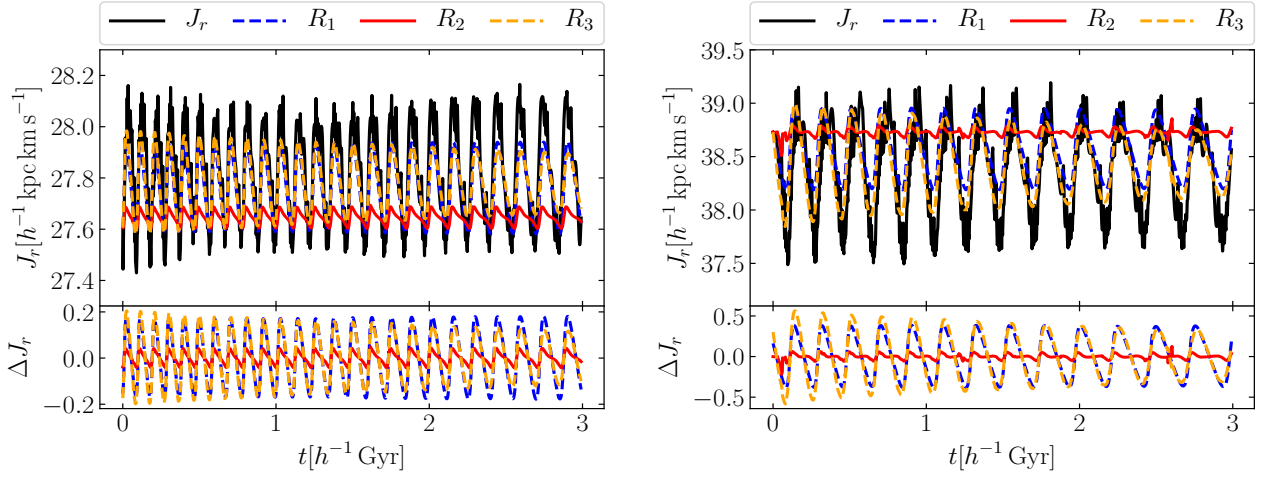


Figure C1. The top panels show the evolution of the radial action of two tracers in a time-dependent Dehnen potential (details in the text). The black line denotes a direct measurement of J_r . The dashed blue line, the solid red line, and the dashed orange line indicate the first order Taylor expansion of J_r (Eq. (19)), using different approximations of the scale factor $R(t)$. In the bottom panels, we show the first order corrections ΔJ_r corresponding to each of the three scale factors.

derivatives as

$$\frac{dR_1}{dt} = -\frac{1}{(3 + \beta(r, t))} \times \left(\frac{F(r, t)}{F(r, 0)} \right)^{-\frac{1}{3 + \beta(r, t)}} \times \left\{ \frac{\dot{F}}{F} - \frac{1}{(3 + \beta(r, t))} \ln \left(\frac{F(r, t)}{F(r, 0)} \right) \times \frac{d\beta}{dt} \right\} \quad (\text{C11})$$

$$\frac{dR_2}{dt} = -\frac{1}{(2 + \alpha(r, t))^2} \times \left(\frac{\Phi(r, t)}{\Phi(r, 0)} \right)^{-\frac{1}{2 + \alpha(r, t)}} \times \left\{ \left[1 - \frac{1}{2 + \alpha(r, t)} \ln \left(\frac{\Phi(r, t)}{\Phi(r, 0)} \right) \right] \times \frac{d\alpha}{dt} + \frac{\dot{\Phi}}{\Phi} \right\} \quad (\text{C12})$$

$$\frac{dR_3}{dt} = -\frac{1}{(2 + \alpha(r, t))^2} \times \left(\frac{\Psi(r, t)}{\Psi(r, 0)} \right)^{-\frac{1}{2 + \alpha(r, t)}} \times \left\{ \left[1 - \frac{1}{2 + \alpha(r, t)} \ln \left(\frac{\Psi(r, t)}{\Psi(r, 0)} \right) \right] \times \frac{d\alpha}{dt} + \frac{\dot{\Psi}}{\Psi} \right\}, \quad (\text{C13})$$

where we take into account that the local power law slopes are in this case time-dependent. Fig. C1 shows the evolution of the radial action of two kinematic tracers, along with the prediction obtained by the first order Taylor expansion using each of the three scale factors. We find that, apart from some numerical issues that occur when calculating the radial action close to the apo- and pericentre of the particle's orbits, the evolution of J_r of both kinematic tracers is accurately described by the Taylor expansion up to linear order, provided we either use R_1 (Eq. (C2)) or R_3 (Eq. (C6)) as the scale factor. In both of these cases, we find that amplitude and period of the oscillation of the radial actions are well described by the Taylor expansion. When comparing the linear correction terms directly (lower panels of Fig. C1), we find that the corrections obtained when using R_1 and R_3 are almost identical. The result of the Taylor approximation using R_2 , however, provides a rather bad description of the evolution of J_r for both tracer particles. This is confirmation that the most important effect here is the changing shape of the potential. Given that in the inner part of the potential, where the impact of the modelled core formation is most substantial, there is a one-to-one correspondence between the logarithmic

slopes of R_1 and R_3 , it is no surprise that they yield very similar values for ΔJ_r . R_2 , however, has the problem that the logarithmic slope is not related to the radial dependence of the force in the innermost region of the potential.

Since there is no physical preference of one scale factor over the other, we conclude that for the purpose of modelling core formation in a SIDM halo, as done in Section 5.2, both R_1 and R_3 can be used to obtain a valid approximation of the evolution of radial actions of particles orbiting in the time-dependent host potential. Small but significant differences between the observed evolution of radial actions and the prediction of our diffusion formalism, as observed in Fig. 15, are thus likely the result of discreteness effects in the N-body simulation.

This paper has been typeset from a $\text{\TeX}/\text{\LaTeX}$ file prepared by the author.